Universidade de Brasília
Instituto de Geociências-IGD
Programa de Pós-graduação em Geologia- PPGG-UnB

DISSERTAÇÃO DE MESTRADO

CARACTERIZAÇÃO MINERALÓGICA E PROVENIÊNCIA DE MONAZITA-(Ce), XENOTIMA-(Y) E ZIRCÃO DE PLACER NA PROVÍNCIA ESTANÍFERA DE GOIÁS: ESTÃO ESTES MINERAIS RELACIONADOS COM O GRANITO TIPO-A SERRA DOURADA?

Deusavan Sales da Costa Filho

Dissertação de Mestrado Nº 463

-Brasília 18 de junho de 2020-

Universidade de Brasília
Instituto de Geociências-IGD
Programa de Pós-graduação em Geologia- PPGG-UnB

DISSERTAÇÃO DE MESTRADO

CARACTERIZAÇÃO MINERALÓGICA E PROVENIÊNCIA DE MONAZITA-(Ce), XENOTIMA-(Y) E ZIRCÃO DE PLACER NA PROVÍNCIA ESTANÍFERA DE GOIÁS: ESTÃO ESTES MINERAIS RELACIONADOS COM O GRANITO TIPO-A SERRA DOURADA?

Deusavan Sales da Costa Filho

18-0097171

Área de Concentração: *Mineralogia e Petrologia*

Orientador: Prof. Dr. Nilson Francisquini Botelho

Banca examinadora:

Profa. Dra. Paola Ferreira Barbosa (UnB)

Prof. Dr. Vitor Paulo Pereira (UFRGS)

Dissertação de Mestrado Nº 463
-Brasília 24 de junho de 2020-

Ficha catalográfica elaborada automaticamente,
com os dados fornecidos pelo(a) autor(a)

Costa Filho, D. c

Costa Filho , Deusavan Sales
CARACTERIZAÇÃO MINERALÓGICA E PROVENIÊNCIA DE MONAZITA (Ce), XENOTIMA-(Y) E ZIRCÃO DE PLACER NA PROVÍNCIA ESTANÍFERA DE GOIÁS: ESTÃO ESTES MINERAIS RELACIONADOS COM O GRANITO TIPO-A SERRA DOURADA? / Deusavan Sales Costa Filho ; orientador Nilson Francisquini Botelho . -- Brasília, 2020.
48 p.

Dissertação (Mestrado - Mestrado em Geologia) -- Universidade de Brasília, 2020.

1. Elementos Terra Raras . 2. Mineralogia . 3. Monasita . 4. Xenotima . 5. Zircão . I. Francisquini Botelho , Nilson , orient. II. Título.

Agradecimentos

A minha mãe Mara Lucia B. de Souza por seu apoio e amor.

Salve minha linhagem preta e feminina
que me mostrou a educação como uma feramente de
mobilização social e transformação pessoal.

Agradeço a todas as professoras e professores
que me inspiraram a cultivar minha curiosidade e dedicação,
principalmente aqueles com quem tive a oportunidade de desenvolver pesquisa,
como a Professora Monica G. Von Huelsen, Alexander Gysi e Welitom Borges

Minha sincera gratidão ao Professor Nilson Botelho, não só pela convivência durante o mestrado mas também pelas aulas de mineralogia durante a graduação. Mesmo perante as adversidades da vida, foram suas aulas que me incentivaram a seguir no curso de geologia.

À memoria de meu pai Deusavan Sales da Costa

Loci Loci Logun!

O presente trabalho foi realizado com apoio da Coordenação de Aperfeiçoamento de Pessoal de Nível Superior - Brasil (CAPES) - Código de Financiamento 001

Resumo

Este estudo apresenta os resultados da caracterização mineralógica e proveniência de monazita-(Ce), xenotima-(Y) e zircão detríticos de um plácer rico em elementos terra raras (ETR) na borda noroeste do Granito da Serra Dourada (GSD) na Província Estanífera de Goiás (PEG). A PEG consiste em dois grupos de granitos do tipo-A de diferentes idades, o g1 (1,77 Ga) e o g2 (1,57 -1,6 Ga). No leste, a Sub-Província Paranã (SPP), composta por granitos g1 e g2, enquanto no Oeste, a Sub-Província Tocantins (SPT), compreendendo apenas os granitos g2, onde o GSD está localizado. As análises por microssonda eletrônica de um conjunto de grãos detríticos resultaram em uma composição mediana compatível com xenotima- (Y) e monazita- (Ce), esse mesmo conjunto de dados apresentam alta dispersão para elementos formadores (Y, Ce e P), além de alta dispersão para actinídeos, especialmente para Th em monazita-(Ce), seguida por uma dispersão moderada de Y e HREE, indicando textura interna complexa formada em estágio pós-magmáticos para os grãos analisados. A textura interna dos ortofosfatos foi investigada por uma combinação de imagens de elétrons espalhados (BSE), EMPA e mapas elementares de raios-X. Os grãos são muito a pouco cristalinos, dependendo do seu conteúdo U e Th, com anomalia negativa de Eu para xenotima. Os dados mostram texturas secundárias complexas que cortam zonas de crescimento magmático devido à sua interação com fluidos ricos em álcalis, F, P, Y, REE durante o estágio hidrotermal relacionado à evolução de um pegmatito da família NYF. Dois tipos de textura de recristalização foram distinguidos pelo processo de dissolução-reprecipitação acopladas, responsável pelo empobrecimento de Th, U e Si e enriquecimento de P, Y, HREE e Ce. Há formação de nano e microporosidade interconectadas, uma vez que o sistema atinge temperaturas hidrotermais (<400 ° C), concomitante à precipitação de nano-inclusões de zircão e micro-inclusões de torita. A datação de um conjunto de grãos de xenotima e monazita detríticos, pelo método U-Pb/LA-ICP-MS, produziu dados concordantes, com uma idade de interceptação de 555 ± 10 e 546 ± 11 Ma, respectivamente. A datação U-Pb LA-ICP-MS de zircão detrítico produziu dados discordantes, com uma idade de intercetação superior de 1609 ± 11 Ma e uma idade de interceptação inferior de 565 ± 11 Ma. Dados mineralógicos e isotópicos, juntamente com os dados da literatura, sugerem o Granito Serra Dourada como fonte de zircão, xenotima e monazita no placer estudado, apesar das idades U-Pb neoproterozóicas dos ortofosfatos. A presença de nano e micro-porosidade interconectadas, combinada ao grau metamórfico de

fácies anfibolíto e o magmatismo granítico da Suíte Mata Azul, associados à orogênese Brasiliana, podem ser os mecanismos responsáveis pela redefinição do relógio U-Pb dos ortofosfatos na SPT.

Palavras-chave: xenotima- (Y); monazita- (Ce); zircão; Granito Serra Dourada (GSD); elementos terras raras (ETR); Província Estanífera do Goiás (PEG); depósitos de plácer.

Abstract

This study presents the results of mineralogical characterizations and provenance of detrital monazite-(Ce), xenotime-(Y) and zircon from an REE-rich placer deposit near the northwestern border of the Serra Dourada granite (SDG) in the Goiás Tin Province (GTP). The GTP consists of two groups of A-type granites of different ages, namely, g1 (1.77 Ga) and g2 (1.57-1.6 Ga). In the east, the Paranã Sub-Province (PSP) consists of g1 and g2 granites, while in the west, the Tocantins Sub-Province (TSP) consists only of g2 granites where the SDG is located. Electron microscopy analyses of a set of orthophosphate detrital grains indicated median xenotime-(Y) and monazite- (Ce) compositions. This same dataset showed high dispersion for forming Y, Ce, P and actinide, especially for Th in monazite-(Ce) and followed by moderate dispersion of HREE, which indicate that complex internal textures formed in the postmagmatic stages of the analyzed grains. The internal textures of orthophosphate were investigated by a combination of backscattered electron (BSE) images, EMPA and X-ray element mapping. They are poorly to strongly crystalline depending on their U and Th contents with significant negative Eu anomalies in xenotime-(Y). They show complex secondary textures that cut magmatic growth zones due to their interactions with F, P, Y, and REE alkali-rich fluids during the hydrothermal stage of NYF pegmatite evolution. Two types of recrystallization textures were distinguished by fluid-aided coupled dissolution-reprecipitation processes in relation to Th, U, and Si depletion and P, Y, HREE and Ce enrichment. Simultaneously, once the system reached hydrothermal temperatures (e.g., <400°C), pervasive and interconnected nano- and microporosity facilitated precipitation of zircon nanoinclusions and thorite microinclusions. U-Pb LA-ICP-MS dating of detrital xenotime and monazite grains yielded concordant data with intercept ages of 555 ± 10 and 546 ± 11 Ma, respectively. U-Pb LA-ICP-MS dating of detrital zircon yielded discordant data, with an upper intercept age of 1,609 ± 11 Ma and a lower intercept age of 565 ± 11 Ma. Mineralogical and isotopic data together with literature data suggest the Serra Dourada granite as the source for zircon, xenotime and monazite in the studied placer, despite the different ages. The pervasive, interconnected nano- and microporosity combined with amphibolite metamorphic grades may be the mechanisms responsible for resetting the orthophosphate U-Pb clock in the TSP.

Keywords: xenotime-(Y); monazite-(Ce); zircon; Serra Dourada Granite (SDG); rare earth elements (REE); Goiás Tin Province (GTP); placer deposits.

Lista de Figuras

Fig. 1 Geological setting of the Serra Dourada Granite: A-Tocantins Province and surrounded cratons: Amazonian (AC), São Francisco (SFC), and Parapanema (or Rio de La Plata) (PRC); B- Goiás Tin Province (GTP) and the sub-provinces: Paranã (PSP) and Tocantins (TSP); C-Serra Dourada Granite and sample location near the northwest border (red triangle); D- detailed sample location in the São Bento creek. 5

Fig. 2 BSE image with EPMA spots in green (A), compositional WDS X-ray maps (B-I), and sketch (J-L) presenting the evolution of the investigated Xn-A grain. Note the U, Th, and Si, heterogenous mirrored patterns, exposing the internal structure. (Thr: thorite inclusions). 12

Fig. 3 BSE image with EPMA spots in green (A), compositional WDS X-ray maps (B-I), and sketch (J-L) presenting the evolution of the investigated Xn-B grain . Note the U, Th, and Si, heterogenous mirrored patterns exposing the internal structure. (Thr: thorite inclusions) 13

Fig. 4 BSE image (A), compositional WDS X-ray maps (B-I), and sketch (J-L) presenting the evolution of the investigated Mz-A. Note the U, Th, and Si, heterogenous mirrored patterns exposing the internal structure. (Thr: thorite inclusions). 16

Fig. 5 BSE image (A), compositional WDS X-ray maps (B-I), and sketch (J-L) presenting the evolution of the investigated Mz-B grain . Note the U, Th, and Si, heterogenous mirrored patterns exposing the internal structure. (Thr: thorite inclusions) 17

Fig. 7 Age cumulative probability plot of $^{206}Pb/^{238}U$(8.A); U-Pb isotopic data for differents xenotime (8-B), zircon (8-D), and monazite (8-C) crystals obtained by Laser Ablation-Inductively Coupled Plasma-Mass Spectrometry. MSWD and probability of the concordia plots are of data concordance plus equivalence (c + e). MSWD = mean square weighted deviation. 20

Fig. 8 Y contents of the studied monazites on the $X_Y^{monazite}$-temperature plot for the monazite limb of the experimentally determined miscibility gap between monazite and xenotime, adapted from Gratz and Heinrich (1997). T< 400°C, for Mz-III and Xn-IV intergrowth, and >500°C, for Mz-I and Mz-II hypothetically coexisting with xenotime. 22

Fig. 9 Summary sketch of xenotime and monazite evolution from magmatic to hydrothermal stage (adapted from Švecová et al., 2016). 24

Fig. 10 Rare earth element patterns for the studied xenotime crystals (light-blue pattern) and xenotime from different origins: (a) metamorphic (Franz et al. 1996; Rasmussen et al. 2011) ; (b) igneous (Kositcin et al. 2003; Rasmussen et al. 2011); (c) hydrothermal (Kositcin et al. 2003; Lan et al. 2013); and (d) diagenetic (Kositcin et al., 2003; Rasmussen et al., 2011). Concentrations were normalized by the chondrite values from McDonough and Sun (1995). 25

Fig. 11 Binary plots of formula proportions of (REE + Y + P) vs. (Th + U + Si) calculated on the basis of 4 oxygen atoms for xenotime and monazite. The huttonitic substitution ((Th, U)$SiREE_{-1}P_{-1}$; Föerster 1998) and cheralitic substitution (Ca(Th, U)REE_{-2}; Linthout 2007) are represented by dashed lines). The proposed direct substitution mechanism corresponds to $4REE^{3+} \leftrightarrow 3(Th,U)^{4+}$ + vacancies (Podor 1996). 26

Fig.12: Summary of ages in the Goiás Tin Province domain. Zr-G1(SPP) and Zr-G2 suites (SPT) (Pimentel et al. 1991); Mz-G1(SPP) and Mz-G2 suites (SPT) (Teixeira and Botelho 2002); Zr-Peixe Alkaline Complex (Kitajima et al. 2002); Mz-Mata Azul Suite (Queiroz e Botelho 2018). 30

Fig. 13: Chondrite-normalized REE patterns for the Serra Dourada and Mata Azul granites. PE samples are from the Pela Ema tin deposit region: PE-1. biotite granite which hosts albitites; PE-2. mineralized albitite; PE-3. mineralized biotite- muscovite granite; PE- 6. biotite granite (Marini et al. 1992). P-1 (Queiroz and Botelho, 2018). 30

A

Fig 1: A,B and C- euhedral to anhedral tetragonal dipyramidal short prisms of light yellow to dark brown xenotime (~ 400-1000 µm); D-euhedral to anhedral prismatic reddish brown to light yellow monazite (~ 350-1200 µm) 48

Fig2: Backscattered electron images of detrital euhedral to anhedral prismatic zircon (~ 100-200 µm). 49

Lista de Tabelas

Table 1. EMPA analyses of detrital xenotime (Xn) and monazites (Mz) grains. Note: nd = below EMP detection limit; STDEV = standard deviation (σ) ***11***

Table 2. EMPA analyses of xenotime (Xn) in samples Xn-A and Xn-B. Note: nd = below EMP detection limit. ***12***

Table 3. EMPA analyses of zircon (Zr-I) in sample Xn-B. Note: nd = below EMP detection limit. ***13***

Table 4. EMPA analyses of monazites in samples MZ-A and MZ-B ***17***

Table 5. Temperature estimated utilizing the monazite-xenotime miscibility gap geothermometer of Heinrich et al. (1997), Gratz and Heinrich (1997, 1998), and Andrehs and Heinrich (1998). ***18***

Annex 1

Table 1: MC-LA-ICPMS U-Pb Xenotime data of SM1. Common lead corrections were applied in the calculation of isotope ratios and ages by using measured 204Pb. All errors are reported on a 2s basis. f206: fraction of common 206Pb; ***40***

Table 2: MC-LA-ICPMS U-Pb monazite data of SM1. Common lead corrections were applied in the calculation of isotope ratios and ages by using measured 204Pb. All errors are reported on a 2s basis. f206: fraction of common 206Pb. ***42***

Table 3: MC-LA-ICPMS U-Pb zircon data of SM1. Common lead corrections were applied in the calculation of isotope ratios and ages by using measured 204Pb. All errors are reported on a 2s basis. f206: fraction of common 206Pb. ***44***

Sumário

Capítulo 1 – Introdução e Justificativa 1

Objetivos e Justificativa 1

Capítulo 2 – Artigo 2

1.0 Introduction 2

2.0 Geological Setting Error! Bookmark not defined.

3.0 Sample and Analytical Methods Error! Bookmark not defined.

3.1 Electron probe microanalysis (EPMA) **Error! Bookmark not defined.**

3.2 Laser ablation inductively coupled plasma mass spectrometry (LA-ICP-MS) **Error! Bookmark not defined.**

4.0 Results 10

4.1 Orthophosphates Chemical Composition Range 10

4.2 Internal Texture of the Orthophosphates and Mineral Inclusions 10

4.2.1 Xenotime 10

4.2.2 Zircon Inclusions 12

4.2.3 Monazite 15

4.2.4 Thorite Inclusions 21

4.3 Isotopic Provenance 23

5.0 Discussion 21

5.1 Crystallization conditions 21

5.2 Regional Implications 30

7.0 References 32

Annex 1 37

Annex 2 47

Capítulo 1 – Introdução e Justificativa

Os ortofosfatos de terras raras REE(PO4), onde REE representa os lantanídeos + Y, existem na natureza principalmente como monazita-(Ce) e xenotima-(Y). Monazita (Ce) incorpora terras raras leves (LREE; La-Gd) enquanto xenotima (Y) tende a incorporar terras raras pesados (HREE; Tb-Lu + V). Essas fases são minerais acessórios em granitos e formam soluções sólidas não ideais (Gysi et al. 2016). São as principais fontes primárias de obtenção de terras raras (Ni et al. 1995). As maiores aplicações de REE em termos de valor agregado são em ímãs e fósforos luminescentes.

No Brasil, importantes alvos de ocorrência de ortofosfatos estão relacionados a granitos do tipo A da Província Estanífera de Goiás (PEG), inicialmente descritos e caracterizados como importantes concentradores de terras raras por Marini e Botelho (1986) e Marini et al. (1992), e recentemente investigados dentro de um grande projeto apoiado pelo CNPq-CT MINERAL (Bastos Neto & Botelho, 2013). O projeto aborda granitos da região de Pitinga, no Amazonas, e granitos da Província Estanífera de Goiás (PEG), na qual se insere esta proposta de Dissertação de Mestrado. Estudos recentes (Santana, 2013; Santana et al. 2015, Costa et al., 2020) abordam o comportamento desses minerais pesados durante seu transporte no ambiente detrítico e saprolítico, principalmente nos maciços Pedra Branca, Serra Dourada e Serra do Encosto (Fig. 1).

Objetivos e Justificativa

Nesta Dissertação de Mestrado propõe-se a caracterização mineralógica e a proveniência isotópicas de xenotima-(Y), monazita-(Ce) e zircão de um plácer localizado junto à borda noroeste do Granito Serra Dourada. O foco da pesquisa é identificar a fonte primária dos minerais detríticos ricos em ETR, usando métodos não destrutivos como EPMA e SEM, combinados com geocronologia de U-Pb LA-ICP-MS. Estudos anteriores em placers próximos ao maciço de granito (Teixeira e Botelho, 2002; Santana et al., 2015) relacionam sua origem a rochas de granito, apesar das idades contraditórias encontradas na monazita. Este estudo tem como objetivo contribuir para a discussão desta questão controversa, uma vez que é importante para a compreensão do potencial de plácer ricos em ETR, hospedados dentro e fora do GSD.

Capítulo 2 – Artigo

MULTI-STAGE EVOLUTION, RESET OF THE U/Pb SYSTEM AND PROVENANCE OF XENOTIME-(Y) AND MONAZITE-(CE) FROM A PLACER DEPOSIT NEAR THE A-TYPE REE-BEARING SERRA DOURADA GRANITE, GOIÁS TIN PROVINCE, BRAZIL

Deusavan Sales da Costa Filho e Nilson Francisquini Botelho
Universidade de Brasília, Instituto de Geociências, Brasília, DF 70910-900, Brazil

1.0 Introduction

Rare earth orthophosphates (REEPO4, where REE is a rare earth element, e.g., lanthanides plus yttrium and scandium) are an important primary source of rare earths and thorium. They also contain significant amounts of uranium (Wark and Miller 1993; Bea 1996a and 1996b). Their anhydrous forms are monazite and xenotime in which stabilization of these two phases depends directly on the nature of the REEs. For the light elements La to Eu, only the monazite structure has been detected in experiments. For the middle-range 4f elements Gd, Tb, and Dy, both monazite and xenotime structures can be encountered. Compounds containing heavier REEs from Ho to Lu and Y only occur in xenotime structures (Gausse et al. 2016).

Due to their typically high U and Th contents and commonly low Pb contents as well as their low Pb diffusivities (Parrish 1990; Vasconcelos et al. 2018), monazite and xenotime are valuable chronometers for dating a wide range of geological processes (e.g., diagenesis (Rasmussen 2005), magmatic crystallization (Hetherington and Harlov 2008; Švecová et al. 2016), metamorphism (Rasmussen et al. 2011; Aleinikoff et al. 2012), and/or hydrothermal mineralization (Lan et al. 2013). In metamorphic and/or felsic magmatic rocks, xenotime may buffer the Y and HREE contents of coexisting minerals and thus provide a basis for geothermometry (Heinrich et al. 1997; Andrehs and Heinrich 1998; Seydoux-Guillaume et al. 2002)

The Serra Dourada A-type granite (SDG) presents primary enrichment in REEs, as was first reported in the 1980s and 1990s by Marini & Botelho (1986) and Marini et al. (1992), who indicated REE contents of 1,000 times the mean chondritic values. Secondary deposits include monazite- and xenotime-rich placers as well as ion-adsorption deposits enriched with up to 1.2 wt% and 0.11 wt% of REE-Y oxides, respectively (Santana et al. 2015).

This study presents the results of an investigation of detrital monazite, xenotime and zircon from a placer deposit near the northwestern border of the SDG. The focus of this research is to identify the primary source of the detrital REE-bearing minerals by using nondestructive EPMA and MEV methods combined with LA-ICP-MS U-Pb geochronology. Previous studies on placers near the granite massif (Teixeira and Botelho, 2002; Santana et al., 2015) related their source to the granitic rocks, despite contradictory ages between monazite and the SDG. This study aims to contribute to the discussion of this controversial issue since it is important for understanding the potential of the SDG for REE placer deposits, which are hosted inside and outside the granite massif.

2 Geological Setting

The studied area is part of the geological context of the Tocantins Structural Province, a unit of first magnitude of the Brazilian geological framework (Almeida et al., 1981; Fuck et al., 2014), located in the central portion of Brazil. This province represented by three main fold belts (Brasília, Araguaia and Paraguai) developed in the Brasiliano Cycle (Neoproterozoic), during the agglutination of western Gondwana, due to the collision of three important cratonic areas: the Amazonian Craton (AC) to the northwest, the São Francisco Craton (SFC) to the east and the supposed Parapanema Craton (or Rio de La Plata Craton; (PRC)) covered by the Paraná basin to the southwest, fig 1.A. At the limit of the Paleo/Mesoproterozoic (1,8 – 1,5 Ga), the basement of the Brasília Fold Belt (BFB), west of SFC, was affected by a statherian tafrogenesis, represented by the Araí Rift, part of the so-called Goiás Tin Province (GTP) fig 1.B.

The Goiás Tin Province (GTP; Figs. 1A and 1B), which is a term coined by Marini and Botelho (1986), consists of twenty granitic bodies and pegmatite dikes. Two groups of A-type granites with different ages occur in this province, namely, the g1 and g2 suites. In the eastern GTP, the Paranã Sub-Province (PSP) consists of g1 and g2 granites while in the west, the Tocantins Sub-Province (TSP) consists only of g2 granites (Botelho & Moura, 1998). The g1 granites formed approximately 1.77 Ga and are related to the syn-rift phase of the Araí Rift while the g2 suite is related to the postrift phase with ages between 1.57 and 1.6 Ga. (Pimentel et al. 1991). Both suites exhibit anomalous enrichment in F, Sn, Rb, Th, U,

Nb, Ga, and REE and they host significant tin deposits which are associated with greisens and pegmatites (Botelho, 1992).

The Serra Dourada granite (SDG) is part of the TSP with Pb-Pb and U-Pb ages between 1.57 and 1.61 Ga (Pimentel and Botelho 2001) and is mainly composed of a biotite granite with minor to less-evolved amphibole-bearing facies. Its main facies consist of quartz, perthitic orthoclase, oligoclase-albite and biotite. Zircon, apatite, monazite-(Ce), xenotime, fluorite and ilmenite are the main accessory minerals (Bilal et al., 1997; Teixeira and Botelho, 1999). The SDG, as well as other A-type granites of the Goiás Tin Province, is considered to be a subvolcanic intrusion with Rapakivi affinities which was emplaced at pressures between 0.5 and 1 kbar which is in accordance with other A-type subvolcanic intrusions related to the Rapakivi series (Botelho, 1992; Bilal et al., 1997; Lenharo et al., 2000; Dall'Agnoll et al. 1999; Bonin, 2007). Marini et al. (1992) drew attention to the REE concentrations in several granites in the Goiás Tin Province, including the Serra Dourada granite, where recent studies have led to characterization of the first REE ion-adsorption deposit in Brazil (Rocha et al., 2013; Santana et al., 2015).

The SDG, fig 1C, is deformed at the borders with a mid to upper amphibolite metmorphism, giving rise to schists and mylonitic orthogneiss. This deformational event is related to the Brasiliano Cycle and generated kilometric envelopes of metasedimentary rocks into a brachianticlinal structure, where the foliation is concentric towards the center of the granite massif. Granites and pegmatites of the the Mata Azul suite crosscut all the preview rocks and are represented by 560 Ma post-collisional intrusions. The bulk composition of the Mata Azul evolved granites and pegmatites consist of quartz, K-feldspar, and muscovite, and the main accessory minerals are garnet, beryl, tourmaline, albite, trilithionite and Fe-Mn phosphates (Queiroz and Botelho 2018) (Fig.1.D).

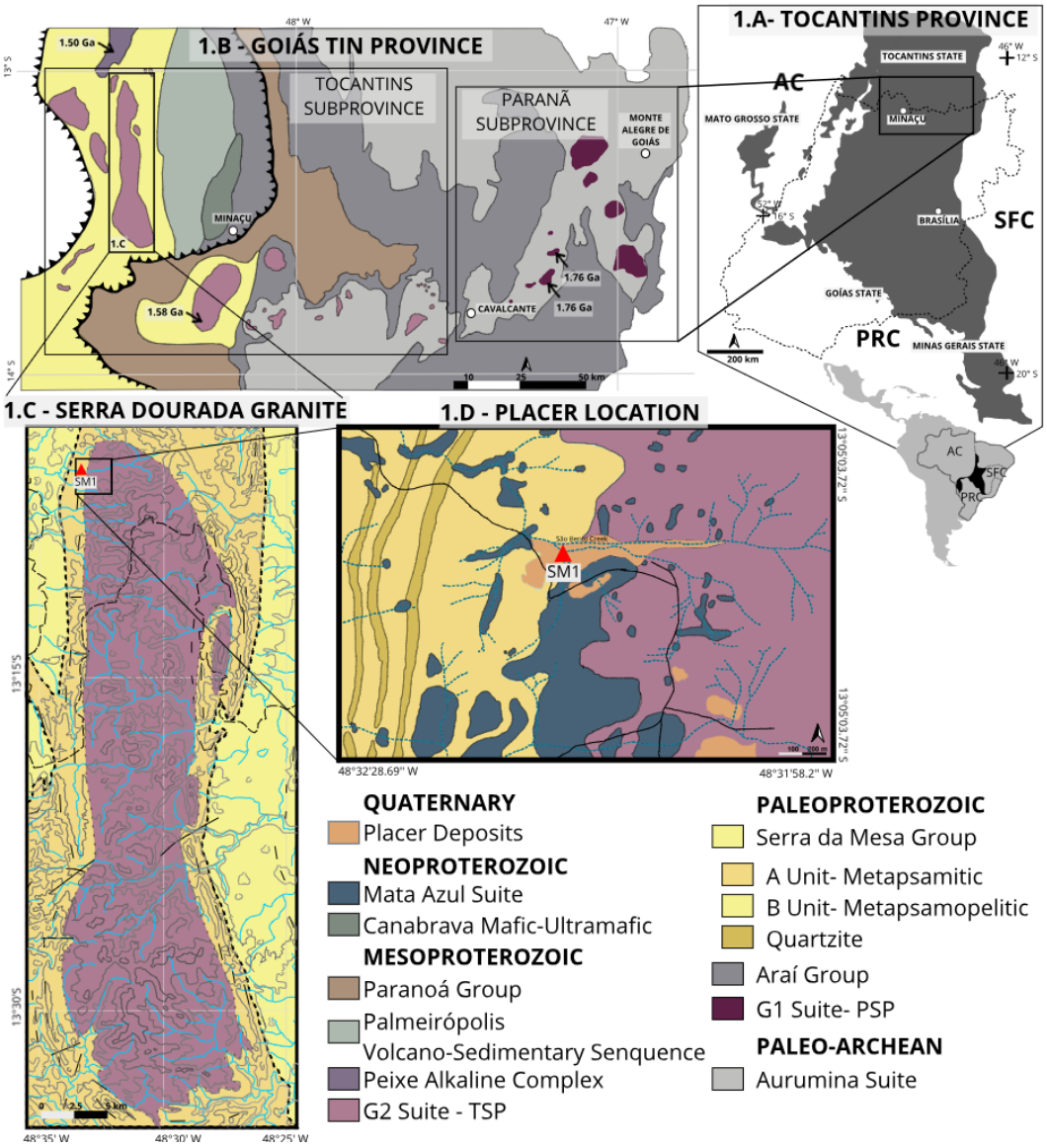

Fig. 1 Geological setting of the Serra Dourada Granite: A-Tocantins Province and surrounded cratons: Amazonian (AC), São Francisco (SFC), and Parapanema (or Rio de La Plata) (PRC); B- Goiás Tin Province (GTP) and the sub-provinces: Paranã (PSP) and Tocantins (TSP); C-Serra Dourada Granite and sample location near the northwest border (red triangle); D- detailed sample location in the São Bento creek.

3 Sample and Analytical Methods

The heavy detrital minerals investigated in this study are from Sao Bento Creek, which is located near the northwestern border of the SDG (Figs. 1C and 1D). The SDG has high relief and is drained by several streams that range from first-order headwaters (>7 km) to small seasonal creeks formed by fluvial downcutting flows. Runoff flows leached the highest (>700 m) weathered domains of the granite massif, deposited the resistant/denser minerals onto downstream flatter areas (<500 m), and formed meter-thickness alluvial deposits. The placer material was sampled during the dry season with a gamma spectrometer to indicate the best sampling points because of the high contents of Th and U of detrital xenotime and monazite. Approximately 200–300 g of material was collected and labeled as SM1 (Fig. 1D).

This material was panned to concentrate its heavy minerals. The minerals that were identified and separated from the concentrate under a binocular lens are euhedral to anhedral tetragonal dipyramidal short prisms of light yellow to dark brown xenotime (~400-1,000 µm); euhedral to anhedral prismatic reddish brown to light yellow monazite (~350-1,200 µm) and euhedral to anhedral prismatic colorless zircon (~100-200 µm) (Fig. 14-15 Annex B). The monazite luster is predominantly resinous but some of its brightness was lost during transport and the grains acquired a matte appearance. Xenotime exhibits more color variations than monazite which are seen as dark yellow to dark brown. The luster is resinous to waxy (Fig. 1 in Annex 2).

3.1 Electron probe microanalysis (EPMA)

Back-scattered electron (BSE), microchemical analyses and X-ray compositional mapping were performed at the University of Brasília using a JEOL JXA-8230. The analytical conditions were as follows: 25 kV acceleration voltage, 50 nA beam current, and beam diameter of 1 µm. The standards were as follows: synthetic glasses for the REE, synthetic oxides of Fe and Y for Y, natural oxides for U and Th, galena for Pb, wollastonite for Ca and Si, and apatite for P. Kα-lines were used for P, Al, Si, Ca and Fe; Lα-lines were used for Y, La, Ce, Er, and Yb; and Lβ-lines were used for Pr, Nd, Sm, Gd, Tb, Dy, and Ho. For U, Th, and Pb, Mβ, Mα and Mβ lines were used, respectively. X-ray element maps were acquired with a step size of 1 µm using a fully focused electron beam, an accelerating voltage

of 20 kV, a probe current of 100 nA, and 100 ms/pixel dwell time. Mapping data were processed using XMapTools 3.4.1 (Lanari et al. 2014; 2019).

3.2 Laser ablation inductively coupled plasma mass spectrometry (LA-ICP-MS)

The methodology and equipment setup used for U-Pb geochronology measurements closely followed those presented by Bühn et al. (2009). Geochronological U-Pb analyses were conducted in the geochronology laboratory at the University of Brasília and used a Thermo Finnigan Neptune multicollector inductively coupled plasma mass spectrometer. Inputs of mineral substances into the spectrometer were achieved by means of the laser ablation technique using a New Wave 213 mm Nd-YAG solid-state laser. A beam diameter of 30 μm and laser energy of ~3.1 J/cm2 at, a frequency of 10 Hz, were used. Samples were inserted into an He-flushed laser chamber with a gas flux between 0.35 and 0.45 l/min. Removal of ^{204}Hg from the He flux was achieved by passing the gas through glass tubes which contained gold-coated quartz particles that were intended to minimize isobaric interference with ^{204}Pb and thus allowed calculations of common lead corrections. For standard and sample analyses, the signals were collected in a single block with 40 cycles of 1.049 s each with signal readings starting after they had attained their maxima following the onset of ablation.

The standard-sample bracketing technique was applied by analyzing one standard spot and one blank for every eight sample spots to account for instrumental drift. The GJ-1 zircon provided by the ARC National Key Centre for Geochemical Evolution and Metallogeny of Continents (GEMOC) of Australia used as the standard. The reference ages of the standard are as follows: ^{207}Pb/^{206}Pb age 1⁄4 608.6 ± 1.1 Ma, ^{206}Pb/^{238}U age 1⁄4 600.4 ± 1.8 Ma, and ^{207}Pb/^{235}U age 1⁄4 602.1 ± 3.0 Ma (Jackson et al., 2004). The USGS 44069 monazite (Aleinikoff et al. 2006) was used as the primary reference material for monazites and the Novo Horizonte xenotime (Chaves et al. 2018) was used as the primary reference material for xenotimes.

Data reduction was achieved using a spreadsheet developed at the geochronology laboratory of Brasília University. This spreadsheet allowed evaluation of isotope ratios for every cycle with a 2 s rejection basis. The corrected ratios and associated calculated ages were displayed using Isoplot 3.75 (Ludwig, 2012).

4.0 Results

4.1 Orthophosphate Chemical Composition Ranges

The chemical compositions ranges of the studied orthophosphates were obtained by random spot analyses of each grain. The 64 grains of detrital xenotime correspond to xenotime-(Y), with Y_2O_3 and P_2O_5 contents ranging from 32.82 to 42.15 wt% and from 22.39 to 34.05 wt%, respectively (Table 1). Dy_2O_3 (2.14 to 4.82 wt%) and Yb_2O_3 (2.75 to 5.11 wt%) are the dominant HREEs. The 24 monazite grains correspond to monazite-(Ce) with Ce_2O_3 and P_2O_5 contents ranging from 30.93 to 38.20 wt% and from 17.20 to 23.62 wt%, respectively (Table 1) while Nd_2O_3 (7.55 to 9.52 wt%) and La_2O_3 (10.33 to 13.01 wt%) represent the highest LREE contents after those of Ce. Furthermore, xenotimes and monazites have high contents of ThO_2 (0.05 to 2.32; 2.32 to 10.78 wt%, respectively) and UO_2 (0.05 to 3.24; 0.39 to 0.89 wt%, respectively). The high standard deviation (σ >145%) for forming elements (e.g., Y, Ce and P) indicates that the grains are composed of different phases. There is also wider range for the actinides (σ >100%), especially for Th in monazite (σ=192%) which reflects fluctuations in actinide contents followed by moderate REE fluctuations.

4.2 Internal Orthophosphate Textures and Mineral Inclusions

The internal textures, mineral inclusions, and chemical compositions of two light-brown euhedral xenotime crystals (Xn-A and Xn-B) and two yellowish euhedral monazite crystals (Mz-A and Mz-B) were investigated by a combination of back-scattered electron (BSE) images and EMPA and X-ray element mapping as shown in Figs. 2 to 5. Three monazite generations (MzI, MzII, and MzIII) and four xenotime generations (Xn-I, Xn-II, Xn-III, and Xn-IV) were identified. Among the mineral inclusions, two zircon generations (ZrI and ZrII) and one thorite generation (Thr-I) were identified (Tables 2-4).

4.2.1 Xenotime

The wavelength-dispersive spectrometry (WDS) X-ray maps (Fig. 2 and 3) represent hexagonal sections of the bipyramidal euhedral crystals Xn-A and Xn-B. Ce, Y, and Pb were mostly homogenous along the rim to core. However, U, Th, and Si displayed heterogenous

mirrored patterns which exposed three distinct intensity signatures. These were medium-intensity euhedral shapes with sharp boundaries, Xn-I (Fig. 2-G); high-intensity with oscillatory zoning parallel to the crystal borders, Xn-II (Fig. 3-G); and low-intensity elongated in the oscillatory zoning direction, Xn-III. The EMPA analyses are presented in Table 2.

Table 1. EMPA analyses of detrital xenotime (Xn) and monazites (Mz) grains. Note: nd = below EMP detection limit; STDEV = standard deviation (σ)

	EMPA-Xn (n=64)					EMPA-Mz (n=47)			
	Median	Range	STDEV.%	D/L ppm		Median	Range	STDEV.%	D/L ppm
CaO	0.06	nd-0.55	14	2012					
SiO_2	0.00	nd-0.55	8	661	**F**	0.64	0-1.56	41	449
P_2O_5	35.43	31.01-37.56	145	457	**CaO**	0.74	0.07-1.91	42	2203
ZrO2	0.79	0.20-4.253	50	1006	**SiO_2**	0.39	0.11-1.74	40	266
Eu_2O_3	0.01	nd-0.114	3	520	**P_2O_5**	27.15	24.09-29.65	157	446
Ce_2O_3	0.15	nd-0.33	7	358	**ZrO_2**	0.52	0.35-0.74	11	1020
Y_2O_3	37.85	32.82-42.15	206	873	**Y_2O_3**	1.88	0.31-3.10	53	821
Gd_2O_3	1.21	0.44-2.10	29	523	**Ce_2O_3**	34.59	30.93-38.20	165	364
Tb_2O_3	0.20	nd-0.45	15	565	**La_2O_3**	11.71	10.33-13.01	77	330
Dy_2O_3	3.94	2.14-4.82	51	1027	**Pr_2O_3**	2.24	1.94-2.46	14	569
Ho_2O_3	0.99	0.72-1.21	12	980	**Sm_2O_3**	1.37	1.08-1.82	19	285
Er_2O_3	3.77	3.16-4.52	25	530	**Nd_2O_3**	8.27	7.55-9.52	6	886
Tm_2O_3	0.67	0.47-0.87	9	586	**Eu_2O_3**	0.52	0.40-0.65	7	520
Yb_2O_3	3.99	2.75-5.11	56	559	**$HREE_2O_3$**	0.92	0.23-1.68	33	555-1046
Lu_2O_3	0.73	0.47-1.03	12	586	**UO_2**	0.66	0.39-0.89	12	215
$LREE_2O_3$	0.77	0.16-1.18	22	208-848	**ThO_2**	4.82	2.32-10.78	192	259
UO_2	2.32	0.5-3.24	46	178	**PbO**	0.06	nd-0.18	6	399
ThO_2	0.92	0.05-2.82	58	206					
PbO	0.03	nd-0.15	5	323					
TOTAL	90.9				TOTAL	99.4			

Xn-I and Xn-II represent early magmatic crystallization with similar chemical compositions and show oscillatory zoning. They were partially replaced via coupled dissolution-reprecipitation by a low-angle reaction front (Fig. 2-K and 3-K) and formed Xn-III in lobate domains. The reprecipitated phase shows enrichment of ~1 wt% by Y, P, Dy and LREE oxides, a Yb_2O_3 increase of ~2 wt% and with the same proportion of ~1 wt%, U, Th oxide decreases. Xn-IV occurs as inclusions in monazite and will be described together with

this mineral.

Table 2. EMPA analyses of xenotime (Xn) in samples Xn-A and Xn-B. Note: nd = below EMP detection limit.

	Xn-II			Xn-III			Xn-IV	
	Median	Range	Cations	Median	Range	Cations	Median	Cations
CaO	0.07	0-0.36	0.000	0.01	nd -0.07	nd	nd	0.000
SiO_2	nd	nd	nd	nd	nd	nd	1.27	0.046
P_2O_5	35.63	35.06-36.41	1.040	36.31	36.29-37.48	1.059	34.23	1.048
ZrO_2	0.77	0.55-0.98	0.013	0.85	0.46-0.94	0.013	1.61	0.028
Ce_2O_3	0.10	0.04-0.14	0.002	0.13	0.09-0.38	0.002	0.39	0.005
Y_2O_3	35.40	34.09-38.84	0.681	37.04	36.14-38.03	0.670	28.68	0.552
Gd_2O_3	1.21	1.11-1.39	0.014	1.30	1.14-1.55	0.015	1.63	0.019
Tb_2O_3	0.34	0.00-0.53	0.005	0.37	0-0.49	0.004	nd	nd
Dy_2O_3	4.28	4.06-4.37	0.049	4.56	4.38-4.82	0.049	5.41	0.063
Ho_2O_3	1.10	0.86-1.15	0.011	1.10	0.97-1.19	0.013	1.17	0.013
Er_2O_3	3.49	3.28-3.8	0.043	3.70	3.49-3.95	0.042	2.31	0.026
Tm_2O_3	0.49	0.44-0.65	0.007	0.50	0.48-0.74	0.007	0.37	0.004
Yb_2O_3	2.74	2.68-3.25	0.053	4.78	2.81-5.10	0.035	2.69	0.030
Lu_2O_3	0.66	0.57-0.78	0.011	0.99	0.64-1.14	0.009	0.74	0.008
$LREE_2O_3$	0.65	0.5-0.94	0.012	0.97	0.70-1.2	0.010	1.04	0.013
UO_2	2.17	1.46-2.34	0.011	1.35	0.45-2.42	0.015	0.58	0.005
ThO_2	0.82	0.53-0.90	0.003	0.43	0.08-0.91	0.005	1.81	0.015
PbO	0.12	nd-0.19	0.001	0.05	nd-0.13	0.001	nd	nd
Total	90.04			94.44			83.93	

4.2.2 Zircon Inclusions

Zircon was observed as a 200 µm euhedral inclusion in the xenotime crystal Xn-B (Zr-I, Fig. 4) and as nanoscale inclusions in xenotime and monazite (Zr-II, Figs. 2-D, 3-D and 6-D). Zr-I is strongly metamictic and has Zr and Y oxides which range between 48.9 and 63.90 wt% and 1.34 to 6.27 wt%, respectively (Table 3). These results indicate that the primary composition was enriched in xenotime molecules, probably via iso-structural-coupled substitutions in Xn-I (Fig. 2-J) and due to the similar shape and size (~250 x 250 µm size), was also considered as an inherited zircon. Moreover, Zr-I crystallized at an early

magmatic stage which was followed by Xn-II overgrowing. Zr-II is restricted to late nanoscale coarse-porosity and vein-like areas marked by enrichment in Si and Zr and the presence of microscale thorite inclusions. eded by Xn-II overgrowing. Zr-II is restricted to a late nanoscale coarse-porosity vein-like areas, marked by enrichment in Si and Zr and presence of microscale thorite inclusions.

Table 3. EMPA analyses of zircon (Zr-I) in sample Xn-B. Note: nd = below EMP detection limit.

	Zr-I				Zr-I		
	Median	Range	Cations		Median	Range	Cations
CaO	0.24	0-1.47	0.009	**Er_2O_3**	0.18	0.16-1.84	0.002
SiO_2	18.65	13.08-22.60	0.646	**Tm_2O_3**	0.00	0.00-0.36	0.000
P_2O_5	3.49	2.20-8.59	0.112	**Yb_2O_3**	0.25	0.3-1.99	0.003
ZrO_2	55.23	48.90-62.90	0.944	**Lu_2O_3**	0.07	0.03-0.45	0.001
Ce_2O_3	0.23	0.19-0.34	0.003	**$LREE_2O_3$**	0.49	0.39-0.61	0.006
Y_2O_3	1.38	1.34-6.27	0.027	**UO_2**	0.57	0.28-0.58	0.004
Gd_2O_3	0.02	0.01-0.14	0.000	**ThO_2**	0.17	0.1-0.77	0.001
Tb_2O_3	nd	0.00	0.000	**PbO**	nd	nd	nd
Dy_2O_3	0.10	0.04-0.41	0.001				
Ho_2O_3	0.12	0.06-0.13	0.001	**Total**	81.18		

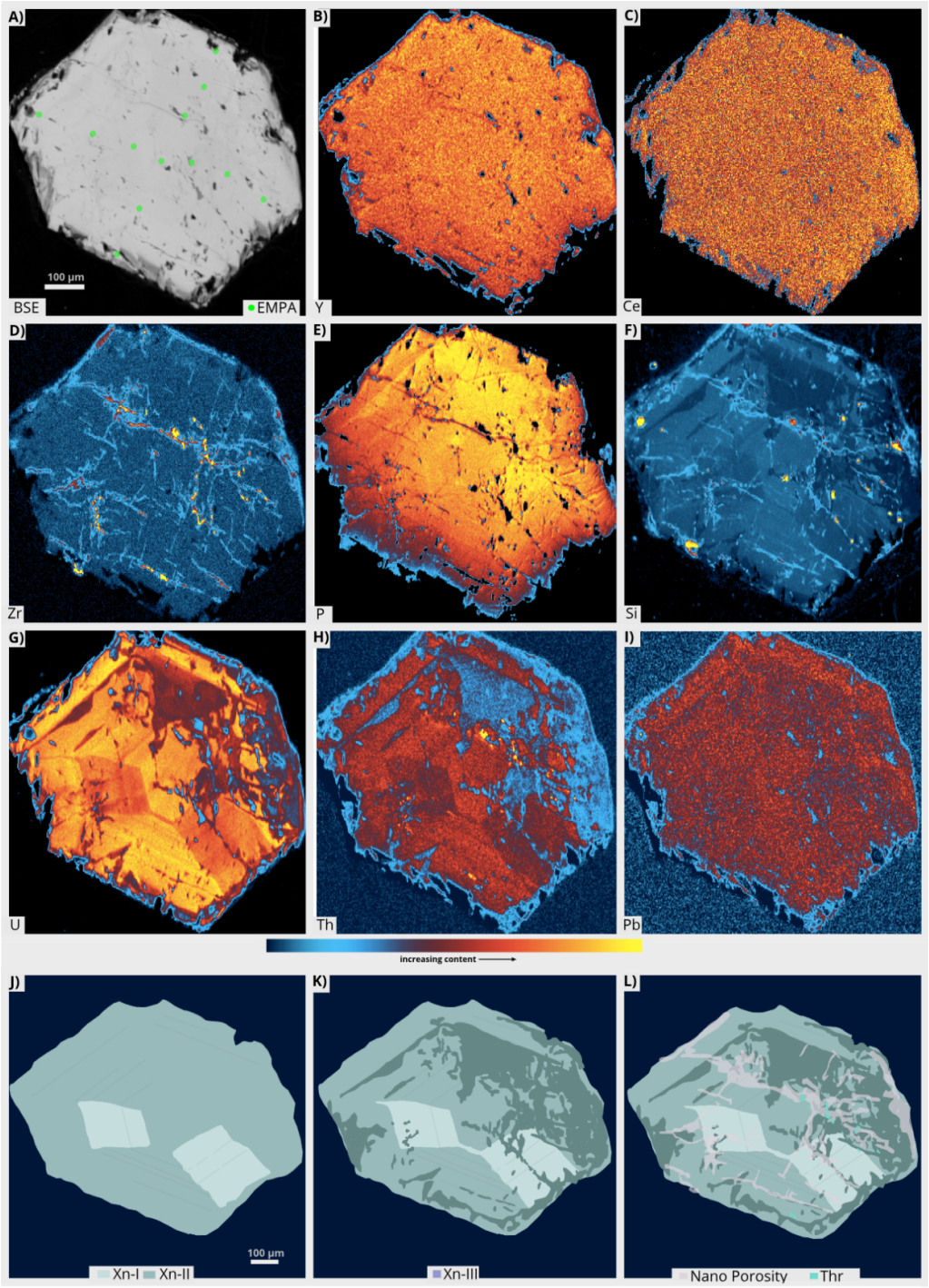

Fig. 2 BSE image with EPMA spots in green (A), compositional WDS X-ray maps (B-I), and sketch (J-L) presenting the evolution of the investigated Xn-A grain. Note the U, Th, and Si, heterogenous mirrored patterns, exposing the internal structure. (Thr: thorite inclusions).

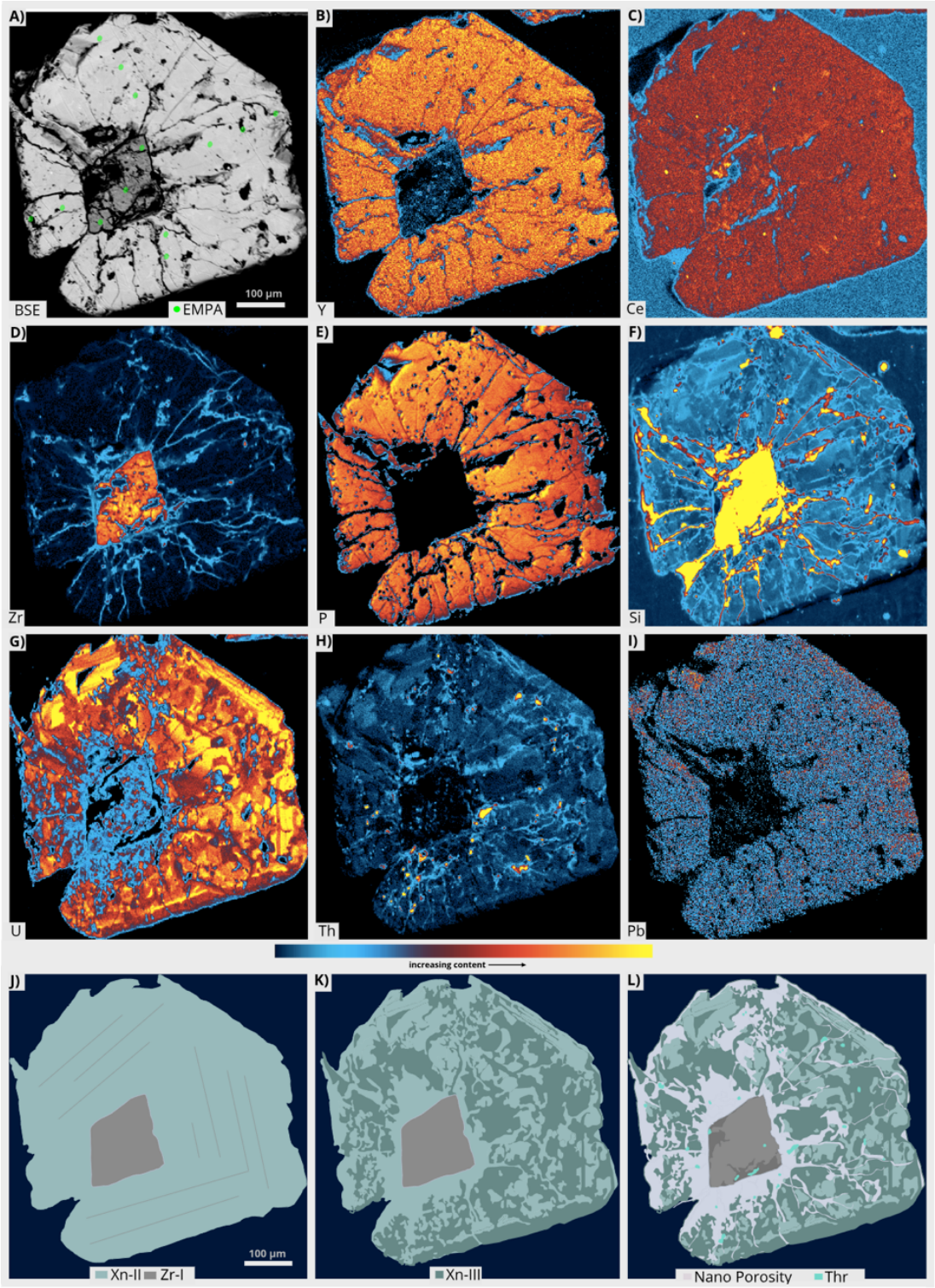

Fig. 3 BSE image with EPMA spots in green (A), compositional WDS X-ray maps (B-I), and sketch (J-L) presenting the evolution of the investigated Xn-B grain . Note the U, Th, and Si, heterogenous mirrored patterns exposing the internal structure. (Thr: thorite inclusions)

4.2.3 Monazite

Crystals Mz-A and Mz-B are elongated prisms cut parallel to the longest growth axis and are ca. 1,138 x 570 μm and ca. 1,095 x 628 μm, respectively. The mirrored Th, U, Si, and Pb contrasting with mirrored Ce and P patterns suggests the existence of three monazite generations (Fig. 4-5). Magmatic monazite (Mz-I) has high concentrations of F, Si, and Th and low values of Ca, P, Y, and HREE (Table 7). Mz-I is partially replaced via coupled dissolution-reprecipitation by Mz-II which formed lobate domains. The reprecipitated MZ-II shows reductions of ~3.3 wt% ThO_2, ~1 wt% Si02 and ~ 0.1 wt% F and enrichment of Ce, Y, and P oxides by ~1 wt%; CaO by 0.5 wt%; and HREE by ~0.25 wt%. Mz-III is considered as a partial replacement via coupled dissolution-reprecipitation and overprinted Mz-II. (Fig. 6-L). In Mz-III, when compared to Mz-II, the ThO_2 content decreased by ~2 wt%, Y_2O_3 by ~1 wt%, and Si and HREE oxides by ~0.5 wt% while the Ce and P oxides increased by ~1 wt%, Sm_2O_3 by 0.5wt%, and F by ~0.2 wt%.

Partial replacement of Mz-II by Mz-III gave rise to precipitation of irregular xenotime (Xn-IV) and displays intergrowths with Mz-III. When compared to Xn-III, Xn-IV shows a Y_2O_3 content that is decreased by ~7 wt% and a Yb_2O_3 content that is decreased by ~2 wt% while Dy_2O_3 is increased by ~1 wt%.

Table 4. EMPA analyses of monazites in samples MZ-A and MZ-B

	MZ-I			MZ-II			MZ-III		
	Median	**Range**	**Cations**	**Median**	**Range**	**Cations**	**Median**	**Range**	**Cations**
F	0.85	0.626-1.068	0.108	0.76	0.62-0.94	0.096	1.05	0.78-1.34	0.133
CaO	0.94	0.47-1.47	0.042	1.36	0.89-2.03	0.061	0.93	0.67-0.93	0.041
SiO_2	1.69	0.4-2.08	0.070	0.54	0.41-1.82	0.022	1.12	0.76-1.36	0.046
P_2O_5	25.87	24.97-27.54	0.912	26.95	25.56-28.07	0.942	26.19	25.74-26.31	0.917
ZrO_2	0.51	0.36-0.75	0.010	0.60	0.48-0.77	0.012	0.58	0.43-0.68	0.012
Y_2O_3	1.63	1.24-1.84	0.035	2.17	1.95-2.38	0.045	0.59	0.49-0.77	0.012
Ce_2O_3	28.17	26.98-30.5	0.428	29.40	27.54-29.4	0.442	29.80	29.09-29.8	0.449
La_2O_3	14.40	13.43-15.63	0.219	14.17	13.67-14.65	0.217	14.26	14.13-14.62	0.216
Pr_2O_3	2.98	2.8-3.3	0.045	3.16	2.78-3.23	0.047	3.16	3.02-3.35	0.048
Sm_2O_3	1.80	1.36-2.22	0.026	1.75	1.55-1.85	0.025	2.14	1.98-2.19	0.031
Nd_2O_3	9.58	8.98-10.26	0.142	10.03	9.15-10.36	0.147	10.37	10.19-10.56	0.154
Eu_2O_3	0.39	0.32-0.46	0.006	0.46	0.32-0.64	0.006	0.40	0.34-0.49	0.006
$HREE_2O_3$	1.08	0.75-1.36	0.014	1.23	1.07-1.43	0.016	0.63	0.12-0.76	0.012
UO_2	0.56	0.44-0.7	0.005	0.54	0.49-0.66	0.005	0.21	0.19-0.27	0.002
ThO_2	10.87	6.08-12.85	0.103	7.56	6.32-12.32	0.070	8.75	8.75-10.45	0.083
PbO	0.15	0.07-0.38	0.002	0.15	0.02-0.26	0.003	0.13	0.08-0.21	0.001
Total	101.48		2.168	100.83		2.157	100.31		2.163

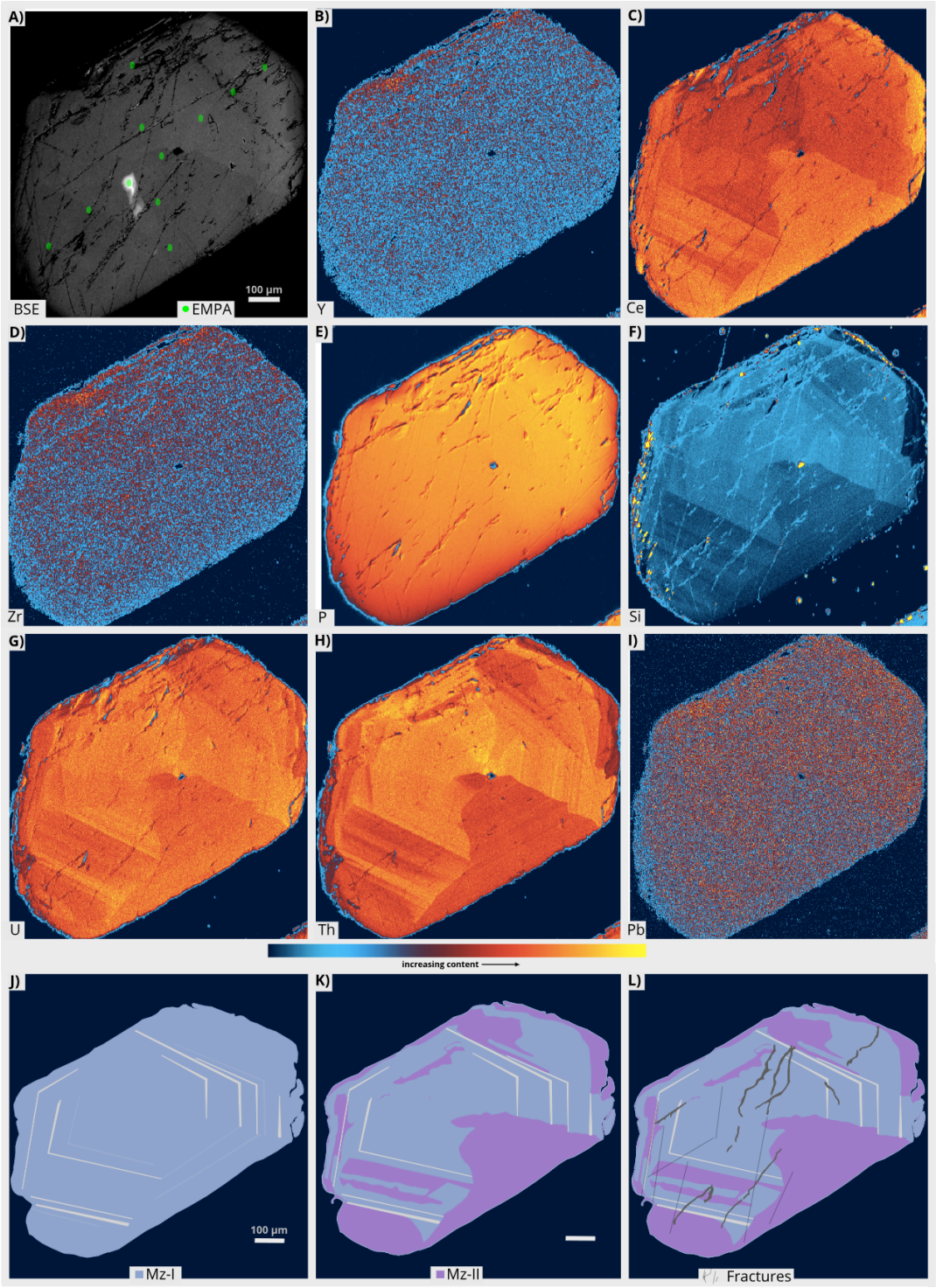

Fig. 4 BSE image (A), compositional WDS X-ray maps (B-I), and sketch (J-L) presenting the evolution of the investigated Mz-A. Note the U, Th, and Si, heterogenous mirrored patterns exposing the internal structure. (Thr: thorite inclusions).

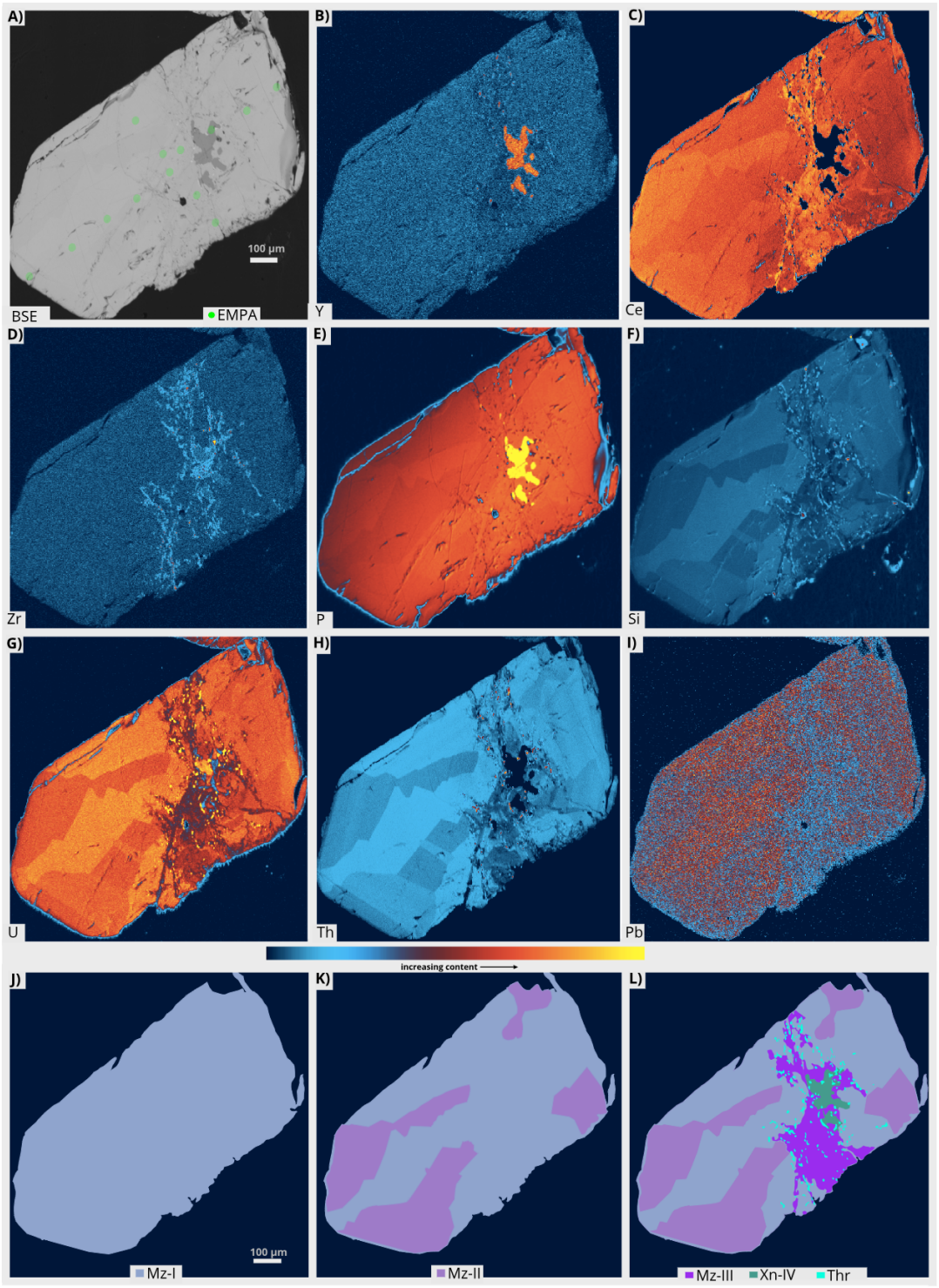

Fig. 5 BSE image (A), compositional WDS X-ray maps (B-I), and sketch (J-L) presenting the evolution of the investigated Mz-B grain . Note the U, Th, and Si, heterogenous mirrored patterns exposing the internal structure. (Thr: thorite inclusions)

4.2.4 Thorite Inclusions

Microscale inclusions of thorite are observed in xenotime and monazite. In xenotime, the inclusions are displayed along planes that are parallel to the crystallographic axes (Fig. 6-top). In monazite, they are restricted to cracks and fractures filled by Th-enriched material (Fig. 6-bottom). Tiny thorite inclusions appeared in equilibrium with the last REE-rich phases, namely, Mz-III and Xn-IV (Fig. 6) and filled the pervasive interconnected nano and microporosities.

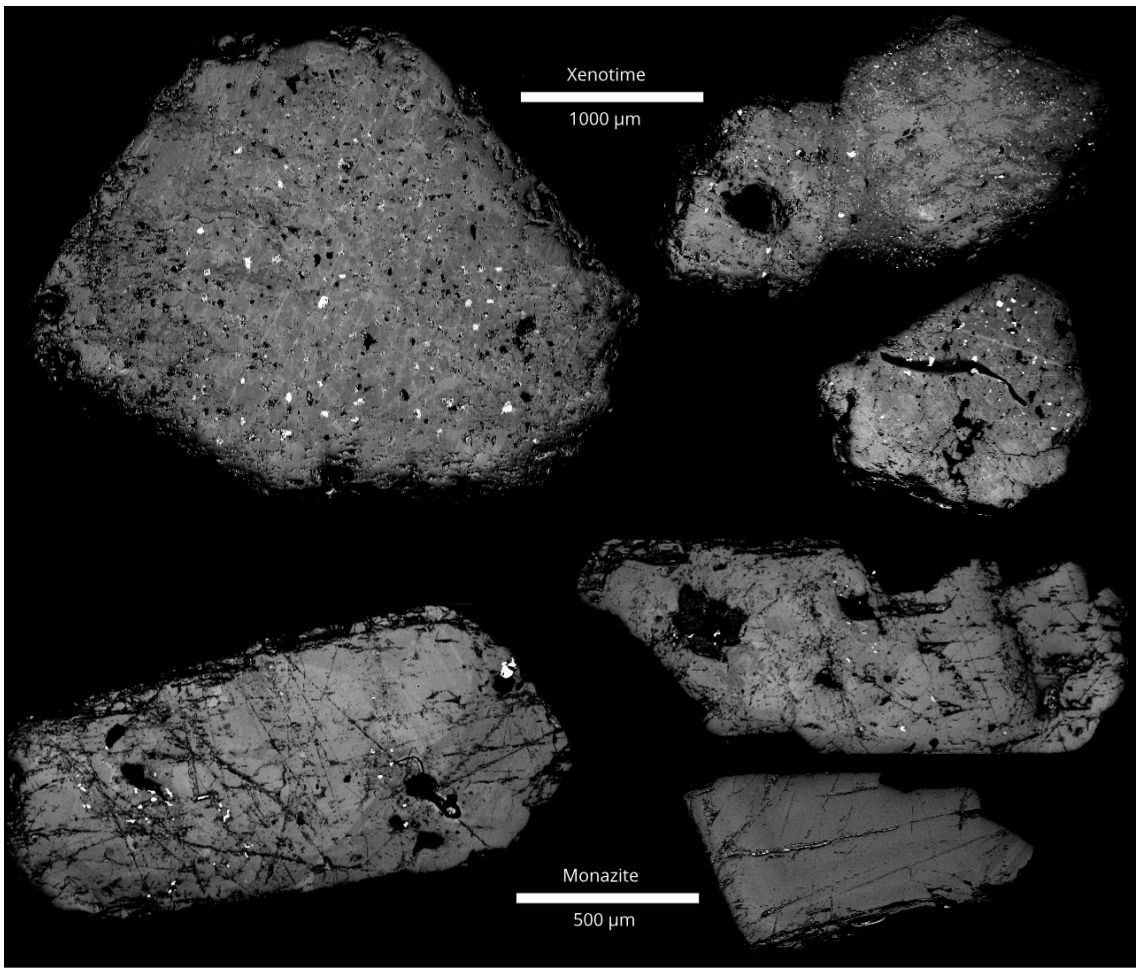

Fig. 6 Backscattered electron images of tiny thorite inclusions (white domains) developed along fractures in xenotime (top) and monazite (bottom). Note the preferred orientation of the distribution of both altered domains (light to dark-gray) and thorite inclusions as well as significant porosity development. Dark-gray domains represent enrichment in REE during metasomatic alteration.

4.3 Isotopic Provenance

Three heavy minerals were identified and separated from the SM1 concentrate for isotopic analyses with the goal of understanding the isotopic provenance of the investigated placer. Age-cumulative probability plots of $^{206}Pb/^{238}U$ data for the analyzed detrital minerals are shown in figure 7A, in which the provenance ages are distributed in two clusters. The younger ages between 510 and 618 Ma are related to xenotime, monazite and zircon while the older ages between 1,500 and 1,700 Ma are related only to zircon. The data for detrital xenotime, monazite and zircon are listed in Annex 1 (Tables 1, 2 and 3, respectively). For the phosphates, there is a significant proportion of data with high analytical errors. In monazite, this is primarily attributable to compositionally zoned crystals. In xenotime, it possibly reflects micronanoscale porosity, cracks, or minor overlap of analytical spots onto micronanoscale porosity. U-Pb LA-ICP-MS dating of xenotime and monazite yielded concordant data with intercept ages of 555 ± 10 Ma and 546 ± 11 Ma, respectively (Fig. 7B-C). U-Pb LA-ICP-MS dating of detrital zircon (Fig. 2 in Annex 2) yielded discordant data with an upper intercept age of 1,609 ± 11 Ma and lower intercept age of 564 ± 11 Ma (n = 48; MSWD = 2.2; Fig. 7D).

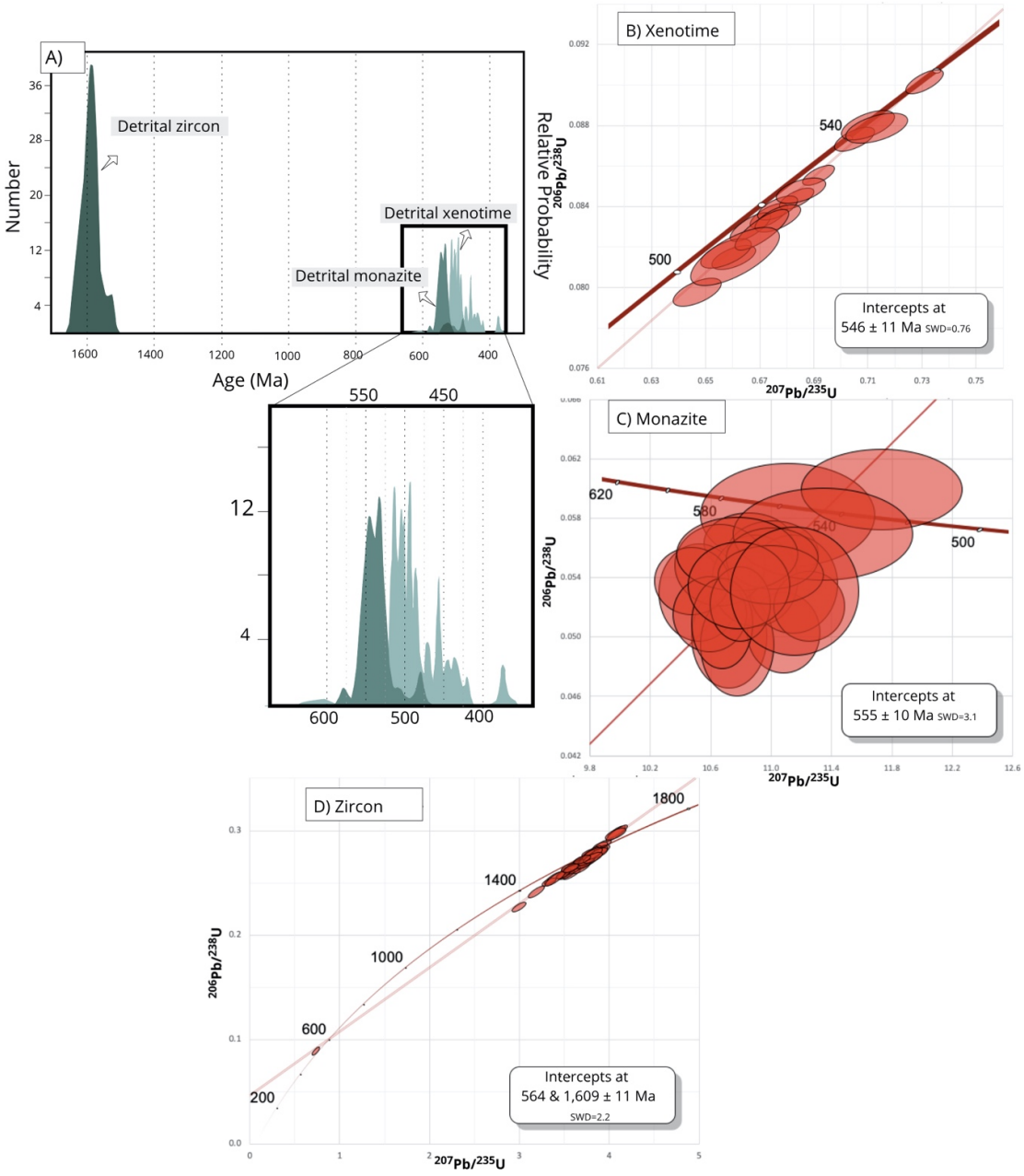

Fig. 7 A) Age cumulative probability plot of $^{206}Pb/^{238}U$; U-Pb isotopic data for differents xenotime B), zircon D), and monazite C) crystals obtained by Laser Ablation-Inductively Coupled Plasma-Mass Spectrometry. MSWD and probability of the concordia plots are of data concordance plus equivalence (c + e). MSWD = mean square weighted deviation.

5.0 Discussion

5.1 Temperature Evaluation

Based on the intergrowth between Xn-IV and Mz-III (Fig. 8), temperatures ranging between 171-372°C at 0.5 kbar were calculated by utilizing the monazite-xenotime miscibility gap geothermometer of Heinrich et al. (1997), Gratz and Heinrich (1997, 1998), and Andrehs and Heinrich (1998). The same geothermometer and pressure were applied to MZ-I and Mz-II and assumed hypothetical coexistence with xenotime and resulted in temperatures ranging between 784-838 °C and 585-748°C, respectively (Table 5). Incorporation of HREE into monazite while coexisting with xenotime increases strongly with temperature and moderately with pressure (Heinrich et al. 1997, Gratz and Heinrich 1997, 1998 and Andrehs and Heinrich 1998). The same authors concluded that only the monazite limb along the monazite-xenotime miscibility gap was appropriate for geothermobarometry. The plot XYMz x T from Gratz and Heinrich (1997) was adopted for pressures below 2 kbar, which was the lowest pressure in these experiments (Fig 8). Pressures between 0.5 and 1 kbar are often estimated for subvolcanic A-type granites, as was mentioned in the SDG geological setting. Temperature estimations are based on XYMz= Y/(Ce+Y) (molar fractions) in Mz-A and Mz-B grains. The plot of estimated temperatures in this diagram (Fig. 8) shows the same range of temperatures that were calculated by utilizing the monazite-xenotime geothermometer of Gratz and Heinrich (1997) and shows that pressure, mainly low pressure, had a moderate influence on the results.

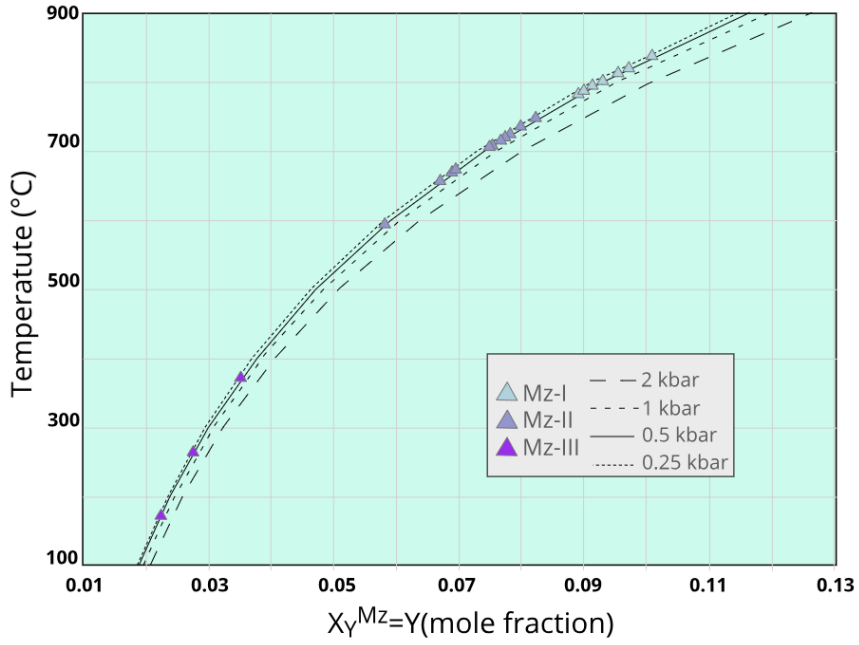

Fig. 8 Y contents of the studied monazites on the $X_Y^{monazite}$-temperature plot for the monazite limb of the experimentally determined miscibility gap between monazite and xenotime, adapted from Gratz and Heinrich (1997). T< 400°C, for Mz-III and Xn-IV intergrowth, and >500°C, for Mz-I and Mz-II hypothetically coexisting with xenotime.

Table 5. Estimated temperatures, utilizing the monazite-xenotime miscibility gap geothermometer of Heinrich et al. (1997), Gratz and Heinrich (1997, 1998), and Andrehs and Heinrich (1998).

	X_Y^{MZ}= Y/Ce+Y	Temperature °C				Y/Ce+Y	Temperature °C		
		P=0.25kbar	P=0.5kbar	P=1kbar			P=0.25kbar	P=0.5kbar	P=1kbar
Mz-I	0.089	790	784	772					
	0.090	794	788	775					
	0.091	801	794	782					
	0.093	808	802	789					
	0.093	808	802	790	Mz-II	0.077	727	721	708
	0.095	820	813	801		0.078	731	725	713
	0.097	828	821	809		0.080	741	735	723
	0.101	844	838	825		0.082	754	748	736
Mz-II	0.058	601	595	583	Mz-III	0.022	178	171	159
	0.067	664	658	646		0.027	271	265	252
	0.069	677	671	659		0.035	378	372	360
	0.069	679	673	661					
	0.075	716	709	697					
	0.075	715	709	696					
	0.076	722	715	703					
	0.077	728	721	709					

5.2 Crystallization conditions

A proposed multistage genetic model for the studied orthophosphates is presented and summarized in Fig. 9. Stage (1) represents an early magmatic stage with crystallization of Zr-I and Xn-I. Zr-I has its primary composition overprinted which resulted in an intermediate zircon-xenotime composition. A-type-derived melts contain highly charged cations such as Nb, Ga, Y and REE in fluoride complexes. The progressive crystallization of amphibole and biotite promotes F partitioning from the melt and causes complex destabilization and accessory mineral precipitation (Collins et al. 1982). For natural samples from the Monte Capanne anatectic-hybrid pluton (Dini et al. 2004), the stability of accessory phases such as monazite, xenotime, and apatite were mainly controlled by Ca activity and degree of melt peraluminosity. From experimental studies, the aluminum saturation index ASI and temperature appear as the determining parameters for the control of monazite/xenotime solubility (Duc-Tin and Keppler 2015).

The presence of chemically homogeneous Xn-I surrounded by zoned U-Th rich Xn-II (Fig. 3-G) probably indicates two-phase magmatic crystallization where Xn-I/Zr-I crystallized from a less evolved melt and were overgrown by Xn-II and precipitated from a more evolved melt (stage 2, Fig. 9). Xenotime overgrowths and intergrowths with zircon as magmatic features were reported in pegmatites by Svecoca et al. (2016) and Budzyń et al. (2018). In addition, the observed high Th, U, and REE contents and significant negative Eu anomalies in the studied xenotimes are consistent with xenotimes from other occurrences in pegmatites (Broska et al. 2005; Hetherington and Harlov 2008; Švecová et al. 2016) and with a magmatic xenotime from Kositein et al. 2003 (Fig. 10).

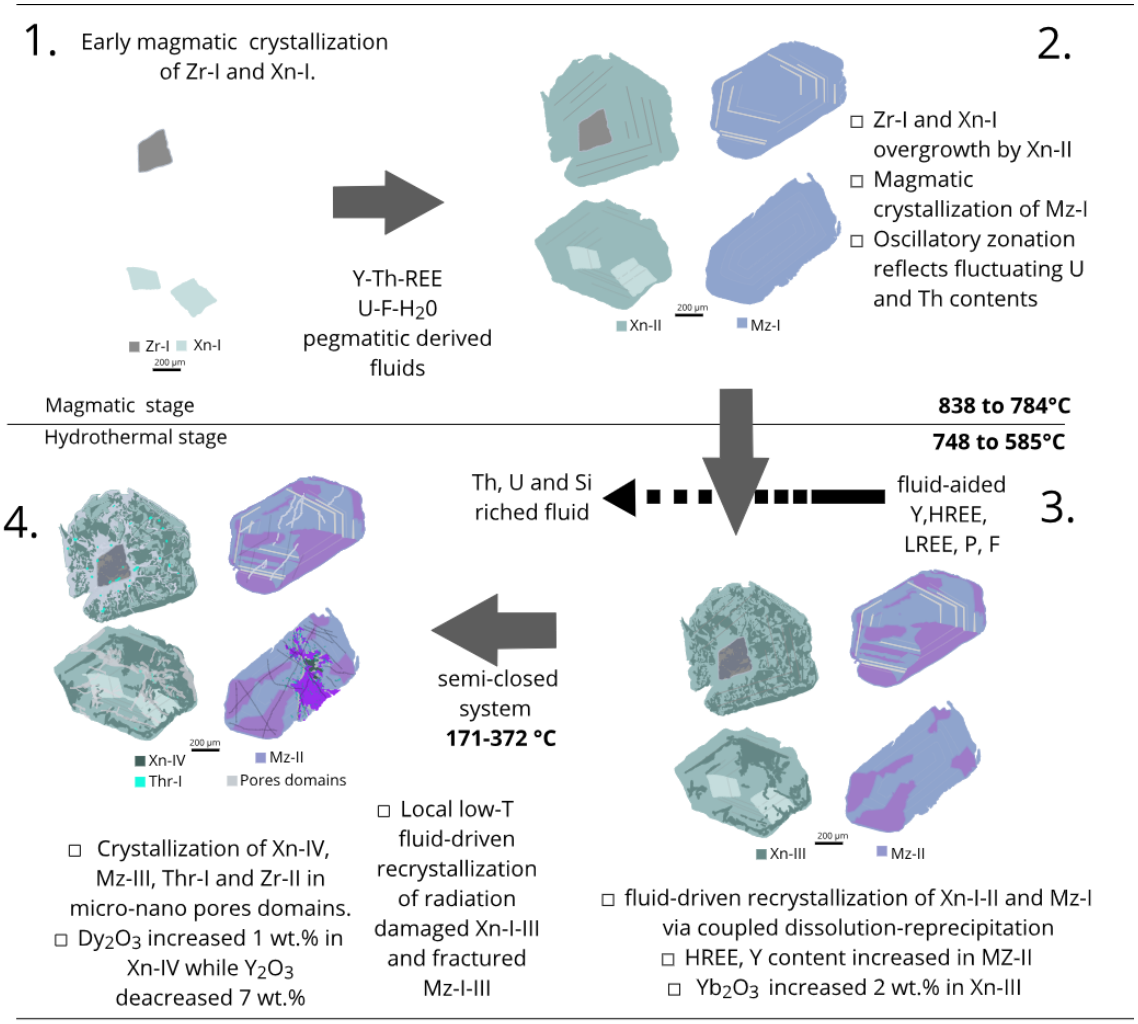

Fig. 9 Summary sketch of xenotime and monazite evolution from magmatic to hydrothermal stage (adapted from Švecová et al., 2016).

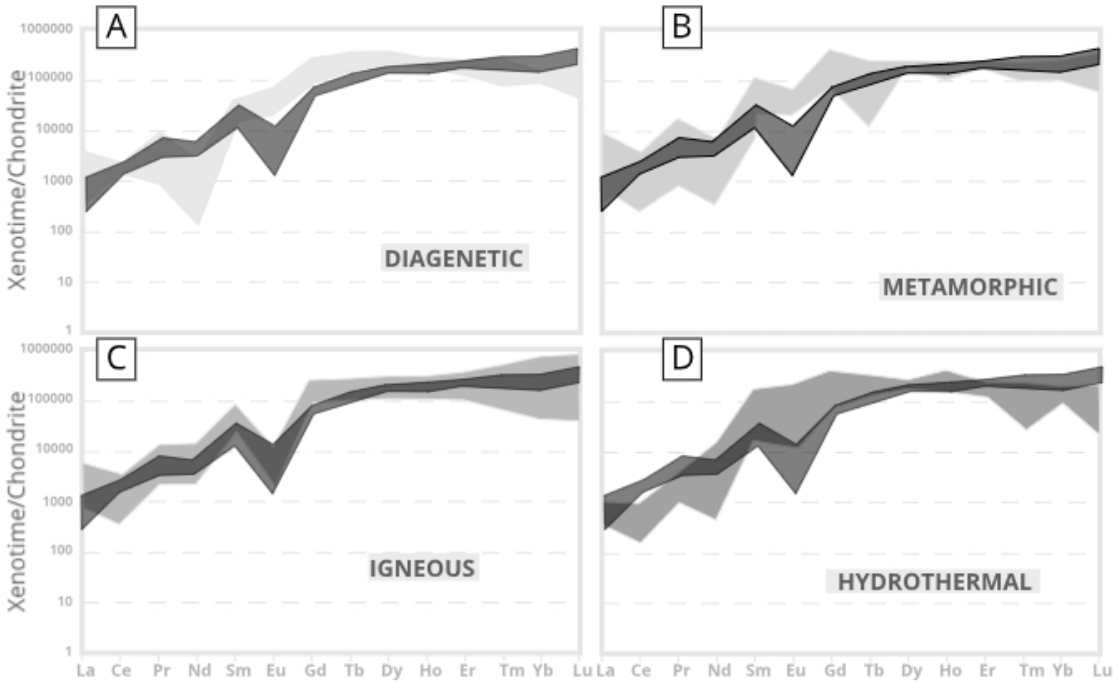

Fig. 10 Rare earth element patterns for the studied xenotime crystals (black pattern) and xenotime from different origins: A) diagenetic (Kositcin et al., 2003; Rasmussen et al., 2011); B) metamorphic (Franz et al. 1996; Rasmussen et al. 2011) ; C) igneous (Kositcin et al. 2003; Rasmussen et al. 2011); and D) hydrothermal (Kositcin et al. 2003; Lan et al. 2013). Concentrations were normalized by the chondrite values from McDonough and Sun (1995).

Incorporation of Th into monazite most commonly occurs due to one of two substitutions: (1) via simple substitution in the A-site with the cheralite endmember [$(Ca,Th)(PO_4)_2$] being defined by the exchange vector $(Ca^{2+})+(Th^{4+})\leftrightarrow(REE^{3+})$ or (2) via an iso-structural coupled substitution on both sites in the crystallographic lattice with the Th-silicate huttonite ($ThSiO_4$) that may be defined by the exchange vector $(Th^{4+})+(SiO4^{-}) \leftrightarrow (REE^{3+})+(PO_{3-})$ (Förster and Harlov 1999). The thorite (ThSiO4) or coffinite (USiO4) component in the xenotime is analogous to the huttonite (ThSiO4) component in solid monazite solutions and a brabantite ($Ca,Th(PO_4)_2$) component is present in both phosphates (Spear and Pyle 2002). The Th-rich Mz-I composition and low CaO concentration indicate that this second exchange huttonite vector defined the compositional variation, see Fig 11. Dini et al. (2004) reported magmatic huttonitic monazites in the Monte Capanne anatectic-hybrid pluton. The same exchange vector may be used to describe the incorporation of actinides into Xn-II and Xn-III which also occurs via an iso-structural coupled substitution with the Th, U-silicate endmember.

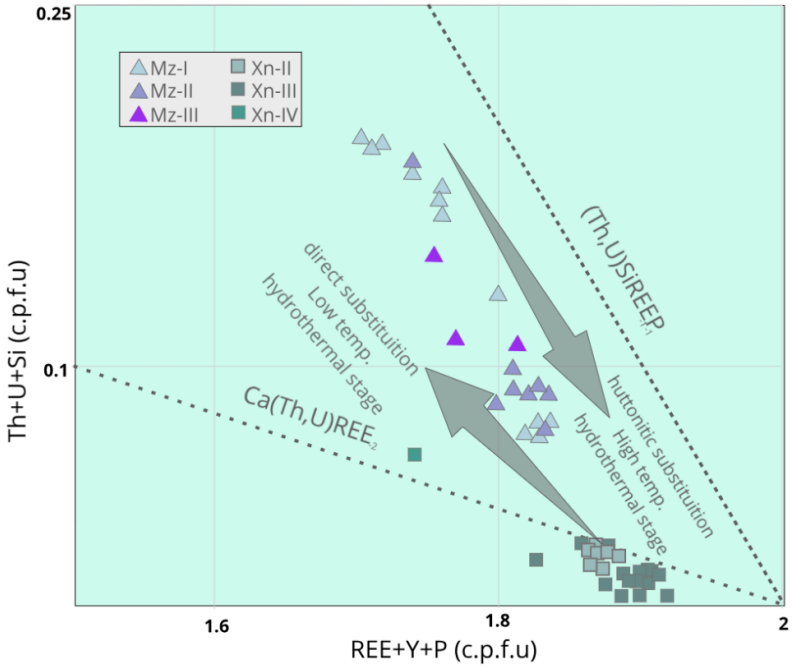

Fig. 11 Binary plots of formula proportions of (REE + Y + P) vs. (Th + U + Si) calculated on the basis of 4 oxygen atoms for xenotime and monazite. The huttonitic substitution ((Th, U)$SiREE_{-1}P_{-1}$; Föerster 1998) and cheralitic substitution (Ca(Th, U)REE_{-2}; Linthout 2007) are represented by dashed lines). The proposed direct substitution mechanism corresponds to $4REE^{3+} \leftrightarrow 3(Th,U)^{4+}$ + vacancies (Podor 1996).

In the monazite and xenotime structures, (LREE)O_9 and (Y,HREE)O_8 polyhedra, respectively, form edge-sharing chains along the crystallographic *a*-axes that are connected by corner-sharing PO_4 tetrahedra (Ni et al. 1995). Edge-sharing chains of alternating PO_4 tetrahedra and Y and REE polyhedra also form along the *c* axis (Ni et al. 1995). Between these chains are interstitial sites that align to form vacancies parallel to the *c* axis (Ni et al. 1995). Direct substitution of trivalent elements by tetravalent actinides with formation of vacancies is reported to occur in natural and synthetic monazites (Peiffert et al. 1996). The proposed mechanism corresponds to $4REE^{3+} \leftrightarrow 3(Th,U)^{4+}$ + vacancies (Podor 1996). Formation of vacancies seems to limit U and Th contents to a few weight percent in natural monazites and for synthetic materials, this limit was determined to be equal to 17.68 wt% ThO_2 (Clavier et al. 2011). Typical values for UO_2 and ThO_2 contents in natural xenotimes range from hundreds of parts per million up to ~6 wt% (Anderson et al. 2019) although higher concentrations have been reported (Förster, 1998; Hetherington et al., 2008; Švecová, et al., 2016).

The interpretation of the magmatic stages (1-2) and hydrothermal stages (3-4) (Fig.

9) is supported by large euhedral crystals with oscillatory zoning which reflect fluctuations in U and Th contents during magmatic crystallization. Further hydrothermal evidence comes from the fluid hydrothermal fingerprinting recorded by fluid-added REE and P but mainly from HREE (stage 3) which was followed by cold fluid-drive recrystallization in a semiclosed system (stage 4). The hydrothermal fluid drive induced two recrystallization microtextures that were ruled out by REE enrichment; Th,U, and Si remobilizations; and negative Eu anomalies.

High-temperature microtextures indicate partial replacement of magmatic phases via coupled dissolution-reprecipitation which resulted in a low-angle inwards rim for Mz-II and metasomatized Xn-III. The hypothetical equilibrium between Mz-II and Xn-III and hot-fluid-added REE and P but mainly HREE are supported by the Mz-II enrichment in Ce, Y, P oxides of ~1 wt%, CaO by 0.5 wt%, and HREE by ~0.25 wt% along with Xn-III enrichment in Y, P, Dy, and LREE oxides of ~1 wt% and in Yb_2O_3 of ~2 wt%. Dissolution-reprecipitation is a chemical process which is driven by minimization of the Gibbs free energy in which a mineral phase in the presence of a reactive fluid is replaced either by an altered composition of the same phase or is replaced by an entirely new phase, e.g., pseudomorphism (Putnis 2002).

Instability of xenotime/monazite in the presence of alkali fluids has been documented in nature (Hetherington and Harlov 2008; Švecová et al. 2016; Budzyń et al. 2018). In experiments, monazite is altered at temperatures from 250 to 550°C (Budzyń et al., 2011, 2015, 2017; Williams et al. 2011) while evidence of small-scale alterations in xenotime was only found at higher temperatures of 550–650°C (Budzyń et al 2018).

In nature, early crystallization of monazite and xenotime was observed in the peraluminous crustally derived A-or S-type (hybrid) pegmatites at Karin Lake, Canada where monazite has a saturation melting temperature which ranges between 625 and 894°C (McKeough et al. 2013). Similarly, the studied Mz-I and MzII have temperatures ranging from 585 to 838°C if they crystallize simultaneously with xenotime. Low-temperature Mz-III has a temperature range between 171 and 372°C (Fig. 9). REE-rich Mz-II has a slightly lower temperature range (585-748°C) than Th-rich Mz-I (784-838°C; Fig. 9). In addition, Y_2O_3 contents increase by 1 wt% in Mz-II followed by the same rate of decrease in the low-temperature Mz-III, which displays intergrowth with Xn-IV.

The internal macrotextures of orthophosphates support the idea that, at high temperatures (>400°C), removal of U, Th and Pb from Th-rich Mz-I and Xn-I-II was induced by fluid-aided coupled dissolution-reprecipitation process and was followed by reprecipitated

REE-rich Mz-II and Xn-III. Once the system reached hydrothermal temperatures (<400°C), the Mz-II structure did not support excesses of HREE or Y, which led to precipitation of the Dy-rich Xn-IV. The Zr, Th, U and Si contents that were removed during the metasomatic stage precipitated simultaneously into pervasive, interconnected nano- and microporosity and yielded zircon nanoinclusions and thorite microinclusions. In xenotime, the hydrothermal stage occurred along planes parallel to the crystallographic axes (Fig. 7-top). However, in monazite, the hydrothermal stage was restricted to cracks and fractures which were filled by Th-enriched material (Fig. 7-bottom). Švecová et al. (2016) reported the same alteration patterns in radiation-damaged xenotime in the Písek pegmatites which resulted in formation of a microporous texture and tiny inclusions of thorite at temperatures >200°C. Budzyń et al (2011) demonstrated preferential partitioning of Th and REE in silicates over phosphates during processes from 250 to 350 °C.

5.3 Regional Implications

The upper intercept age of 1,608 ± 11Ma for detrital zircon from the studied placer indicates the possibility of a Mesoproterozoic source for this placer. Indeed, this provenance age is compatible with the age (1.57 - 1.61 Ga) of the Serra Dourada granite (SDG). Additionally, the immaturity and size (~350-1,200 μm) of the fluvial sediments, which contain predominantly angular and euhedral grains, indicate the proximity of the source rock. Generally, xenotime crystals (20-200 μm) of proposed igneous origin are common among heavy detrital minerals in reef or conglomerate horizons at Witwatersrand Basin, South Africa (Kositcin et al. 2002). In addition, large pegmatitic xenotime crystals from the Písek pegmatites, Czech Republic exhibit similar sizes (>1,000 μm) as the xenotimes in this study. For the xenotimes from these regions, the morphology and internal textures and REE pattern of the studied xenotime with a negative Eu anomaly, are consistent with a magmatic origin. However, the Neoproterozoic ages displayed by monazite and xenotime are not consistent with a direct relationship with the SDG and are more reliable for ages related to the Neoproterozoic Brasiliano Orogenic Cycle.

In the Brasiliano Orogenic Cycle, deeper crustal levels were exhumed by movements on the NE–SW-trending Rio Maranhão Fault System (Soares et al. 2006; D'el-Rey Silva et al. 2008). Consequently, in the eastern part of Goiás Tin Province, the Araí Group and related

A-type magmatism were subjected to lower greenschist facies conditions. Instead, in the western Tocantins Subprovince (TSP), the SMG preserved mid- to upper amphibolite facies (kyanite zone) assemblages. Peak metamorphic conditions of 5-7 kbar and 540°C have been attributed to these rocks (Bilal et al 1997). Teixeira (2002) carried out U-Pb chemical dating on magmatic and hydrothermal monazites from both A-type suites of the Goiás Tin Province and, similar to this study, monazites from both suites have undergone Pb loss and show Neoproterozoic ages. However, in eastern Paranã Subprovince, some monazite crystals have preserved zones with Paleoproterozoic ages. Previous geochronological data available in the context of the Goiás Tin Province and data from this study are summarized in figure 13.

Typically, detrital xenotimes persist in greenschist and upper amphibolite facies conditions (Rasmussen et al. 2011; Williams et al. 2011) as well as monazite (Budzyń et al. 2011). However, as was pointed by Seydoux-Guillaume et al. (2019), Pb diffusion in orthophosphates may be enhanced by radiation damage (e.g., amorphization, metamictization), which is caused by their U and Th contents. In the studied xenotime, metamictization must have facilitated Pb diffusion and thus reset the U-Pb system. According to Hetherington and Harlov (2008), metamictization must be considered as a mechanism that favors porosity formation and gives rise to damaged zones susceptible to dissolution and removal by fluids while leaving behind pores. Despite the fact that monazite is not affected by metamictization due a defect recovery mechanism called α-healing (Seydoux-Guillaume et al. 2018), nanoscale studies of natural monazite not only revealed nanoclusters that were enriched in radiogenic Pb but also demonstrated closed U-Th-Pb geochronological systems at grain scales (μm-scale) but open systems at nano scales in which Pb diffusion cannot be neglected (Seydoux-Guillaume et al. 2019).

The Neoproterozoic LCT leucogranite-pegmatites of the Mata Azul suite can be suggested as the source for the detrital orthophosphates of the studied placer. However, xenotime is not reported in these rocks and their primary monazite yields a U-Pb age of 519 ± 2.8 Ma (Queiroz and Botelho 2018). Additionally, the lower Th (0.6-2.8 ppm), Y (7.2-20.5 ppm) and Ce (2.5-9.1 ppm) contents and geochemical characteristics of the Li-Cs-Ta (LCT) granite-pegmatite group exclude the Mata Azul suite as a possible source of the detrital orthophosphates investigated in this study. On the other hand, the high REEY concentrations in the Serra Dourada biotite granite (Fig. 13) with high contents of Ce (230-323 ppm), Y (76-131 ppm) and Th (43-82 ppm) (Marini et al. 1992; Santana et al, 2015) and its NYF (Nb-Y-

F) signature allow us to suggest this granite massif as the source for the detrital heavy minerals investigated.

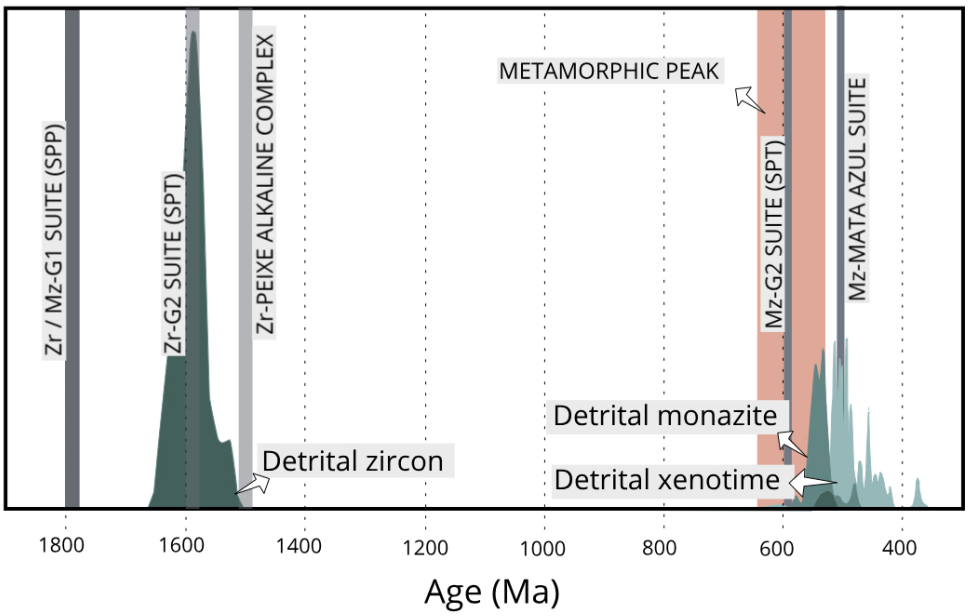

Fig.12: Summary of ages in the Goiás Tin Province domain. Zr-G1(SPP) and Zr-G2 suites (SPT) (Pimentel et al. 1991); Mz-G1(SPP) and Mz-G2 suites (SPT) (Teixeira and Botelho 2002); Zr-Peixe Alkaline Complex (Kitajima et al. 2002); Mz-Mata Azul Suite (Queiroz e Botelho 2018).

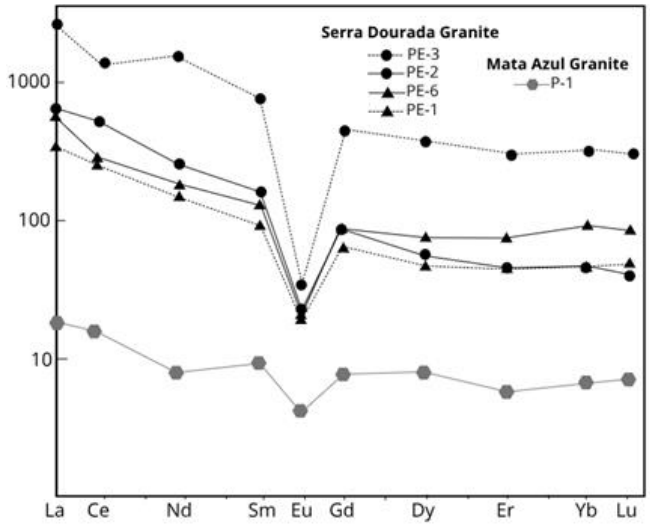

Fig. 13: Chondrite-normalized REE patterns for the Serra Dourada and Mata Azul granites. PE samples are from the Pela Ema tin deposit region: PE-1. biotite granite which hosts albitites; PE-2. mineralized albitite; PE-3. mineralized biotite- muscovite granite; PE- 6. biotite granite (Marini et al. 1992). P-1 (Queiroz and Botelho, 2018).

6.0 Conclusions

The heavy-mineral associations in the studied placer at the border of the Serra Dourada granite (SDG) are mainly composed of monazite–(Ce), xenotime–(Y) and zircon. All of these minerals occur predominantly as euhedral grains with low to absent roundness; morphological and MEV analyses allowed identification of four xenotime generations (Xn-I to Xn-IV) and three monazite generations (Mz-I to Mz-III)

The combination of morphological and EPMA analyses allowed detection of magmatic xenotime (Xn-I) overgrowing relict diamond-shaped zircons and revealed that magmatic REE-phosphates (e.g., Xn-I, Xn-II, and Mz-I) crystallized at temperatures between 784 and 838ºC and have progressive fluid-aided alterations. These alterations are divided in two stages: 1 - partial replacement via coupled dissolution-reprecipitation at temperatures between 585 and 748ºC with new phases (Xn-III; Mz-II, and Mz-III) depleted in Th, U, Si and enriched in REE,P; 2 - total-partial replacement via a fluid-mediated overprint at temperatures between 171 and 372°C including crystallization of hydrothermal xenotimes (Xn-IV) as inclusions which were only observed in monazites and micrometer-scale metasomatic thorite microinclusions and zircon nanoinclusions. The alterations in stage 2 were facilitated by pervasive metamictization in xenotime and interconnected nano- and microporosity which acted as sinks for nanoclusters enriched in radiogenic Pb.

The upper intercept age of 1,609 ± 11 Ma for the detrital zircon is similar to the age attributed to the SDG. The zircon lower intercept age (565 ± 11 Ma) and ages of xenotime and monazite (555 ± 10 and 546 ± 11, respectively) are interpreted as reequilibration/ rejuvenation ages related to the Neoproterozoic Brasiliano Orogenic Cycle. Despite the different ages, this study suggests that the Serra Dourada granite is the source for the zircon, xenotime and monazite in the studied placer. The presence of pervasive, interconnected nano- and microporosity, when combined with an upper amphibolite metamorphic grade, may be the mechanisms responsible for the resetting of the orthophosphate clock in the TSP. The recorded Th-U-total Pb age disturbance in the xenotime did not result in a complete resetting of the Th-U-Pb clock but rejuvenated the metamorphic peak ages and was probably caused by thermal events related to the late Mata Azul Suite (Fig. 12).

7. References

Aleinikoff, J.N., Schenck, W.S., Plank, M.O., Srogi, L.A., Fanning, C.M., Kamo, S.L., and Bosbyshell, H. (2006) Deciphering igneous and metamorphic events in high-grade rocks of the Wilmington complex, Delaware: Morphology, cathodoluminescence and backscattered electron zoning, and SHRIMP U-Pb geochronology of zircon and monazite. Bulletin of the Geological Society of America, 118, 39–64.

Aleinikoff, J.N., Grauch, R.I., Mazdab, F.K., Kwak, L., Fanning, C.M., and Kamo, S.L. (2012) Origin of an unusual monazite-xenotime gneiss, Hudson Highlands, New York: Shrimp U-Pb geochronology and trace element geochemistry. American Journal of Science, 312, 723–765.

Almeida, F.F.M., Hasui, Y., Brito-Neves, B.B., Fuck, R.A. (1981) Brazilian structural provinces: an introduction. Earth-Science Reviews, 17: 1-29.

Anderson, A.J., Hodges, K. V., van Soest, M.C., and Hanchar, J.M. (2019) Helium Diffusion in Natural Xenotime. Geochemistry, Geophysics, Geosystems, 20, 417–433.

Andrehs, G., and Heinrich, W. (1998) Experimental determination of REE distributions between monazite and xenotime: potential for temperature-calibrated geochronology. Chemical Geology, 149, 83–96.

Bastos Neto, A.C. e Botelho, N.F. (2013) Estudo integrado de geologia, mineralogia e caracterização tecnológica do minério no depósito associado ao granito Madeira e em planta piloto, com vistas à exploração de ETRP como coproduto do Sn-Nb-Ta na mina Pitinga (AM). Avaliação do potencial para ETRP de granitos análogos na Província Estanífera de Goiás. Chamada MCTI/CNPq/CT-Mineral Nº 76/2013: APOIO AO DES. TECNOLÓGICO EM TERRAS RARAS. UFRGS/UnB, 45pp**.**

Bea, F. (1996a) Controls on the trace element composition of crustal melts. Transactions of the Royal Society of Edinburgh, Earth Sciences, 87, 33–41.

——— (1996b) Residence of REE, Y, Th and U in granites and crustal protoliths; implications for the chemistry of crustal melts. Journal of Petrology, 37, 521–552.

Bilal, E.; Moute, J.; Botelho, N.F.; Marini, O.J.; Andrade, G.F. (1997) Geochemistry of two Proterozoic A-type Granites of Goiás State. Brazil: possible links with rapakivi series. Annals of the Brazilian Academy of Sciences, 69: 349-365.

Boatner, L.A. (2002) Synthesis, structure, and properties of monazite, pretulite, and xenotime. In M.L. Kohn, J. Rakovan, and J.M. Hughes, Eds., Phosphates —Geochemical, Geobiological, and Materials Importance, 48, p. 87–121. Reviews in Mineralogy and Geochemistry, Mineralogical Society of America, Chantilly, Virginia.

Bonin B. (2007) A-type granites and related rocks: Evolution of a concept, problems and prospects. Lithos 97: 1–29.

Botelho, N.F., (1992) Les ensembles granitiques subalcalins a peralumineux mineralisés en Sn et In de la Sous-Province Paranã , Etat de Goiás, Brésil. Dr. Thesis, Univ. Paris VI, France.

Botelho, N.F., Moura, M.A. (1998) Granite-ore deposit relationships in Central Brazil. J. South Am. Earth Sci. 1, 427–438.

Broska, I., Williams, C.T., Janák, M., and Nagy, G. (2005) Alteration and breakdown of xenotime-(Y) and monazite-(Ce) in granitic rocks of the Western Carpathians, Slovakia. Lithos, 82, 71–83.

Budzyń, B., Hetherington, C.J., Williams, M.L., Jercinovic, M.J., Michalik, M., (2010) Fluid-mineral interactions and constraints on monazite alteration during metamorphism. Min. Mag. 74, 659–681.

Budzyń, B., Harlov, D.E., Williams, M.L., Jercinovic, M.J. (2011). Experimental determination of stability relations between monazite, fluorapatite, allanite, and REE-epidote as a function of pressure, temperature, and fluid composition. American Mineralogist 96,1547-1567.

Budzyń, B., and Kozub-Budzyń, G.A. (2015) The stability of xenotime in high Ca and Ca-Na systems, under experimental conditions of 250-350°c and 200-400 MPa: The implications for fluid-mediated low-temperature processes in granitic rocks. Geological Quarterly, 59, 316–324.

Budzyń, B., Konečný, P., Kozub-Budzyń, G.A. (2015). Stability of monazite and disturbance of the Th–U–Pb system under experimental conditions of 250–350 °C and 200–400 MPa. Ann. Soc. Geol. Pol. 85, 405–424.

Budzyń, B., Harlov, D.E., Kozub-Budzyń, G.A., and Majka, J. (2017) Experimental constraints on the relative stabilities of the two systems monazite-(Ce) – allanite-(Ce) – fluorapatite and xenotime-(Y) – (Y,HREE)-rich epidote – (Y,HREE)-rich fluorapatite, in high Ca and Na-Ca environments under P-T conditions of 200–1000 . Mineralogy and Petrology, 111, 183–217.

Budzyń, B., Sláma, J., Kozub-Budzyń, G.A., Konečný, P., Holický, I., Rzepa, G., and Jastrzębski, M. (2018) Constraints on the timing of multiple thermal events and re-equilibration recorded by high-U zircon and xenotime: Case study of pegmatite from Piława Górna (Góry Sowie Block, SW Poland). Lithos, 310–311, 65–85.

Budzyń, B., and Sláma, J. (2019) Partial resetting of U–Pb ages during experimental fluid-induced re-equilibration of xenotime. Lithos, 346–347.

Bühn, B., Pimentel, M.M., Matteini, M., and Dantas, E.L. (2009) High spatial resolution analysis of Pb and U isotopes for geochronology by laser ablation multi-collector inductively coupled plasma mass spectrometry (LA-MC-ICP-MS). Anais da Academia Brasileira de Ciencias, 81, 99–114.

Chaves, M.L. de S.C., Buhn, B., Heinis Dias, C., and Menezes Filho, L.A.D. (2018). Idades U-Pb em xenotímio-(Y) de um veio de quartzo com almeidaíta e parisita-(La), novos minerais encontrados na Serra do Espinhaço (Novo Horizonte, Bahia). Geociências, 37, 225–236.

Clavier, N., Podor, R., and Dacheux, N. (2011) Crystal chemistry of the monazite structure. Journal of the European Ceramic Society, 31, 941–976.

Collins, W.J., Beams, S.D., White, A.J.R., and Chappell, B.W. (1982) Nature and origin of A-type granites with particular reference to southeastern Australia. Contributions to Mineralogy and Petrology, 80, 189–200.

Costa, N.O., Botelho, N.F., Garnier, J. (2020) Concentration of rare earth elements in the Faixa Placha tin deposit, Pedra Branca A-Type Granitic Massif, central Brazil, and its potential for ion adsorption- type REE-Y mineralization. Ore Geol. Rev., 123: 103606.

Dall'Agnol, R., Costi, H.T., Leite, A.A., Magalhães, M.S., Teixeira, N.P., 1999. Rapakivi granites from Brazil and adjacent areas. Precambr. Res. 95: 9-36

D'el-Rey Silva, L.J.H., de Vasconcelos, M.A.R., and Silva, D.V.G. (2008) Timing and role of the Maranhão River Thrust in the evolution of the Neoproterozoic Brasília Belt and Tocantins Province, central Brazil. Gondwana Research, 13, 352–374.

Dini, A., Rocchi, S., and Westerman, D.S. (2004) Reaction microtextures of REE-Y-Th-U accessory minerals in the Monte Capanne pluton (Elba Island, Italy): A possible indicator of hybridization processes. Lithos, 78, 101–118.

Duc-Tin, Q., and Keppler, H. (2015) Monazite and xenotime solubility in granitic melts and the origin of the lanthanide tetrad effect. Contributions to Mineralogy and Petrology, 169, 1–26.

Franz, G., Andrehs, G., and Rhede, D. (1996) Crystal chemistry of monazite and xenotime from Saxothuringian-Moldanubian metapelites, NE Bavaria, Germany. European Journal of Mineralogy, 8, 1097–1118.

Föerster, H.-J. (1998) The chemical composition of {REE}-{Y}-{Th}-{U}-rich accessory minerals in peraluminous granites of the {Erzgebirge}-{Fichtelgebirge} region, {Germany}; {Part} {I}, {The} monazite-({Ce})-brabantite solid solution series. American Mineralogist, 83, 259–272.

Förster, H.-J. and Harlov, D.E. (1999) Monazite-(Ce)-huttonite solid solutions in granulite-facies metabasites from the Ivera-Verbano Zone, Italy. Mineralogical Magazine.

Fuck, R.A., Dantas, E.L., Pimentel, M.M., Botelho, N.F., Armstrong, R., Laux, J.H., Junges, S.L., Soares, J.E., Praxedes, I.F. 2014. Paleoproterozoic crust-formation and reworking events in the Tocantins Province, central Brazil: A contribution for Atlantica supercontinent reconstruction. Precambrian Research, 244: 53–74.

Gausse, C., Szenknect, S., Qin, D.W., Mesbah, A., Clavier, N., Neumeier, S., Bosbach, D., and Dacheux, N. (2016) Determination of the Solubility of Rhabdophanes LnPO4·0.667H2O (Ln = La to Dy). European Journal of Inorganic Chemistry, 2016, 4615–4630.

Gratz, R. and Heinrich, W. (1997) Monazite-xenotime thermobarometry: experi- mental calibration of the miscibility gap in the binary system CePO4-YPO4. American Mineralogist, 82, 772–780.

——— (1998) Monazite-xenotime thermometry. III. Experimental calibration of the partitioning of gadolinium between monazite and xenotime. European Journal of Mineralogy, 10, 579–588.

Gysi, A.P., Williams-Jones, A.E., and Collins, P. (2016) Lithogeochemical Vectors for Hydrothermal Processes in the Strange Lake Peralkaline Granitic REE-Zr-Nb Deposit. Economic Geology, 111, 1241–1276.

Harlov, D.E. (1999) Monazite-group minerals in granulite-facies metabasites from the Ivrea – Verbano Zone , N . Italy: implications for high grade fluid flow.

Heinrich, W., Andrehs, G., and Franz, G. (1997) Monazite – xenotime miscibility gap thermometry . I . An empirical calibration. Journal Metamorphic Geology, 15, 3–16.

Hetherington, C.J., and Harlov, D.E. (2008) Metasomatic thorite and uraninite inclusions in xenotime and monazite from granitic pegmatites, Hidra anorthosite massif, southwestern Norway: Mechanics and fluid chemistry. American Mineralogist, 93, 806–820.

Jackson, S.E., Pearson, N.J., Griffin, W.L., Belousova, E.A., 2004. The application of laser ablation inductively coupled plasma mass spectrometry to in situ U-Pb zircon geochronology. Chem. Geol. 211, 47e69.

Kitajima, L. F. W., Ruiz, J. Gehrels, G., GASPAR, J. C.(2001) Uranium-Lead ages of zircon megacrysts and zircon included in corundum from Peixe Alkaline Complex (Brazil). In: III Simposio Sudamericano de Geologia Isotopica, 2001, Pucón. III Simposio Sudamericano de Geologia Isotopica.

Kositcin, N., McNaughton, N.J., Griffin, B.J., Fletcher, I.R., Groves, D.I., and Rasmussen, B. (2003) Textural and geochemical discrimination between xenotime of different origin in the Archaean Witwatersrand Basin, South Africa. Geochimica et Cosmochimica Acta, 67, 709–731.

Lanari, P., Vidal, O., De Andrade, V., Dubacq, B., Lewin, E., Grosch, E., Schwartz, S. (2014) XMapTools: a MATLAB©-based program for electron microprobe X-ray image processing and geothermobarometry. Computers and Geosciences. 62, 227-240.

Lanari, P., Vho, A., Bovay, T., Airaghi, L., Centrella, S., (2019) Quantitative compositional mapping of mineral phases by electron probe micro-analyser. Geological Society of London, Special Publications, 478, 39-63

Lan, Z.W., Chen, Z.Q., Li, X.H., Li, B., and Adams, D. (2013) Hydrothermal origin of the Paleoproterozoic xenotime from the King Leopold Sandstone of the Kimberley Group, Kimberley, NW Australia: Implications for a ca 1.7 Ga far-field hydrothermal event. Australian Journal of Earth Sciences, 60, 497–508.

Lenharo, S.L.R., Moura, M.A., Botelho, N.F., 2002. Petrogenetic and mineralization processes in Paleo- to Mesoproterozoic rapakivi granites: examples from Pitinga and Goias, Brazil. Precambr. Res. 119, 277.

Linthout, K. (2007) Tripartite division of the system 2REEPO4-CaTh (PO4)2-2ThSiO4, discreditation of brabantite, and recognition of cheralite as the name for members dominated by CaTh(PO4)2. Canadian Mineralogist, 45, 503–508.

Ludwig, K.R., 2012. Isoplot. A Geochronological Toolkit for Microsoft Excel. Ver. 3.75. Berkeley Geochronology Center.

Marin, O.J., and Botelho, N.F. (1986) A província de granitos estaníferos de Goiás. Revista Brasileira de Geociências, 1, 119–131

Marini, O.J., Botelho, N.F., and Rossi, P. (1992) Elementos Terras Raras Em Granitóides Da Província Estanífera De Goiás. Revista Brasileira de Geociências, 22, 61–72.

McDonough, W.F., and Sun, S. s. (1995) The composition of the Earth. Chemical Geology, 120, 223–253.

Ni, Y., Hughes, J.M., and Mariano, A.N. (1995) Crystal chemistry of the monazite and xenotime structures tetrahedra and RE polyhedra , with a REOg polyhedron in xenotime that accommodates the heavy lanthanides (Tb-Lu in the synthetic phases) and a RE09 polyhedron in monazite that preferentially inco. American Mineralogist, 80, 21–26.

Parrish, R.R. (1990) U-Pb dating of monazite and its application to geological problems. Canadian Journal of Earth Sciences, 27, 1431–1450.

Peiffert C., Brouand M., Cuney M., and Podor R. La monazite—de l'indicateur de fertilité des granites pour les granites. Rapport CEA 1996: 103–8.

Pimentel, M.M., and Botelho, N.F. (2001) Sr and Nd isotopic characteristics of 1.77-1.58 Ga rift-related granites and volcanics of the Goiás tin province, Central Brazil. Anais da Academia Brasileira de Ciencias, 73, 262–276.

Pimentel, M.M., Heaman, L., Fuck, R.A., and Marini, O.J. (1991) U-Pb zircon geochronology of Precambrian tin-bearing continental-type acid magmatism in central Brazil. Precambrian Research, 52, 321–335.

Podor R. (1994) Synthèse et caractérisation des monazites uranifères et thorifères. PhD Thesis of Université Henri Poincaré, Nancy (France) (N◦ 94 NAN10404).

Putnis, A. (2002) Mineral replacement reactions: from macroscopic observations to microscopic mechanisms. Mineralogical Magazine, 66, 689–708.

Queiroz H.A. and Botelho N.F. 2017. The Mata Azul pegmatitic field, Tocantins/Goiás, central Brazil: geology, genesis and mineralization. Brazilian Journal of Geology, 48(3): 435-456.

Rasmussen, B. (2005) Radiometric dating of sedimentary rocks: The application of diagenetic xenotime geochronology. Earth-Science Reviews, 68, 197–243.

Rasmussen, B., Fletcher, I.R., and Muhling, J.R. (2011) Response of xenotime to prograde metamorphism. Contributions to Mineralogy and Petrology, 162, 1259–1277.

Salvi, S., and Williams-Jones, A.E. (1991) The role of hydrothermal processes in the granite-hosted Zr, Y, REE deposit at Strange Lake, Quebec/Labrador: Evidence from fluid inclusions. Geochimica et Cosmochimica Acta, 55, 3447–3449.

Salvi, S., and Williams-Jones AE (2005) Alkaline granite-syenite deposits. In: Linnen RL, Samson IM (eds) Rare Element Geochemistry and Mineral Deposits. Geological Association of Canada Short Course Notes 17, pp 315-341

Santana, I. V., Wall, F., and Botelho, N.F. (2015) Occurrence and behavior of monazite-(Ce) and xenotime-(Y) in detrital and saprolitic environments related to the Serra Dourada granite, Goiás/Tocantins State, Brazil: Potential for REE deposits. Journal of Geochemical Exploration, 155, 1–13.

Santana,, I.G. 2013 Caracterização Mineralógica e Geoquímica de Ocorrências de Terras Raras no Maciço Granítico Serra Dourada, Goiás/Tocantins, Brasil. M. Sc. Dissertation,, Universidade de Brasília, 69 p.

Seydoux-Guillaume, A.-M., Wirth, R., Heinrich, W., and Montel, J.-M. 2002 Experimental determination of Thorium partitioning between monazite and xenotime using analytical electron microscopy and X-ray diffraction Rietveld analysis. European Journal of Mineralogy, 14, 869–878.

Seydoux-Guillaume, A.-M., Deschanels, X., Baumier, C., Neumeier, S., Weber, W.J., Peuget, S., 2018. Why natural monazite never becomes amorphous: experi- mental evidence for alpha self-healing. American Mineralogist 103, 824e827.

Seydoux-Guillaume, A.M., Fougerouse, D., Laurent, A.T., Gardés, E., Reddy, S.M., and Saxey, D.W. (2019) Nanoscale resetting of the Th/Pb system in an isotopically-closed monazite grain: A combined atom probe and transmission electron microscopy study. Geoscience Frontiers, 10, 65–76.

Soares, J.E., Berrocal, J., Fuck, R.A., Mooney, W.D., and Ventura, D.B.R. (2006) Seismic characteristics of central Brazil crust and upper mantle: A deep seismic refraction study. Journal of Geophysical Research: Solid Earth, 111, 1–31.

Spear, F.S., and Pyle, J.M. (2002) Apatite, monazite, and xenotime in metamorphic rocks (in Phosphates; geochemical, geobiological, and materials importance) Reviews in Mineralogy and Geochemistry. Reviews in Mineralogy and Geochemistry, 48, 293–335.

Švecová, E., Čopjaková, R., Losos, Z., Škoda, R., Nasdala, L., and Cícha, J. (2016) Multi-stage evolution of xenotime–(Y) from Písek pegmatites, Czech Republic: an electron probe micro-analysis and Raman spectroscopy study. Mineralogy and Petrology, 110, 747–765.

Teixeira L.M., Botelho N.F. (1999). Comportamento dos elementos terra raras pesados em zircão, xenotima e torita de granitos e greisens da subprovíncia estanífera Paranã- Goiás. Brazilian Journal of Geology, **29**:549-556

Teixeira, L.M. (2002) Caracterização de Minerais Portadores de Terras Raras e sua Aplicação à Petrologia e Geocronologia de Granitos das Subprovíncias Tocantins e Paranã – Goiás. PhD Thesis, University of Brasília, Brazil, 356 p.

Vasconcelos, A.D., Gonçalves, G.O., Lana, C., Buick, I.S., Kamo, S.L., Corfu, F., Scholz, R., Alkmim, A., Queiroga, G., Nalini, H.A. (2018) Characterization of Xenotime From Datas (Brazil) as a Potential Reference Material for In Situ U-Pb Geochronology. Geochemistry, Geophysics, Geosystems, 19, 2262–2282.

Wark, D.A., Miller, C.F. (1993) Accessory mineral behavior during differentiation of a granite suite: monazite, xenotime and zircon in the Sweetwater Wash pluton, southeastern California, U.S.A. Chemical Geology, 110, 49–67.

Williams, M.L., Jercinovic, M.J., Harlov, D.E., Budzyń, B., Hetherington, C.J. (2011) Resetting monazite ages during fluid-related alteration. Chemical Geology, 283, 218–225.

Annex 1

1

Table 1: MC-LA-ICPMS U-Pb Xenotime data of SM1. Common lead corrections were applied in the calculation of isotope ratios and ages by using measured 204Pb. All errors are reported on a 2s basis. f206: fraction of common 206Pb;

Identifier	206* (%)	204Pb cps	206Pb mV1	Th/U	206Pb/204Pb	1s%	207Pb/206Pb	1s %	207Pb/235U	1s %	206Pb/238U	1s %	Rho	207Pb/206Pb	2s abs	206Pb/238U	2s abs	207Pb/235U	2s abs	% U-Pb disc
004-XN2	0.04	471.46	0.20	0.29	34800.07	9.35	0.06	0.40	0.66	0.52	0.08	0.30	0.58	553.27	17.26	504.47	2.95	513.34	4.20	8.82
008-XN6	0.01	112.95	0.16	0.34	111196.85	11.12	0.06	0.22	0.69	0.36	0.09	0.25	0.67	550.99	9.68	528.94	2.49	533.06	3.02	4.00
010-XN8	0.01	157.23	0.28	0.23	118305.92	6.04	0.06	0.31	0.70	0.44	0.09	0.28	0.63	548.99	13.37	539.63	2.86	541.37	3.69	1.71
012-XN10	0.04	652.16	0.41	0.33	41930.91	6.18	0.06	0.46	0.71	0.59	0.09	0.34	0.57	547.41	19.94	543.81	3.53	544.45	4.96	0.66
018-XN14	0.00	94.06	0.27	0.40	1307770.29	60.06	0.06	0.28	0.67	0.44	0.08	0.30	0.69	542.30	12.17	516.88	3.01	521.55	3.58	4.69
019-XN15	0.02	129.73	0.18	0.34	95004.53	7.98	0.06	0.25	0.68	0.39	0.08	0.26	0.66	554.71	10.96	521.97	2.62	528.06	3.24	5.90
021-XN17	0.02	186.74	0.13	0.42	67229.05	14.40	0.06	0.28	0.66	0.48	0.08	0.36	0.74	534.44	12.41	513.43	3.53	517.26	3.90	3.93
024-XN20	0.03	171.34	0.12	0.18	46514.00	4.76	0.06	0.33	0.67	0.47	0.08	0.29	0.63	543.39	14.36	519.17	2.92	523.63	3.81	4.46
032-XN24	0.00	62.61	0.17	0.30	934119.26	51.24	0.06	0.25	0.73	0.40	0.09	0.27	0.69	559.82	10.75	556.71	2.92	557.27	3.42	0.56
038-XN30	0.05	433.87	0.16	0.33	31098.51	8.90	0.06	0.45	0.64	0.59	0.08	0.36	0.61	554.01	19.36	493.98	3.41	504.73	4.70	10.83
041-XN31	0.12	1327.48	0.26	0.53	12854.45	4.18	0.06	0.39	0.67	0.53	0.08	0.34	0.63	557.10	16.78	516.13	3.34	523.70	4.37	7.36
046-XN36	0.00	63.84	0.16	0.38	947802.52	46.41	0.06	0.46	0.65	0.61	0.08	0.37	0.61	538.08	19.98	505.63	3.63	511.50	4.90	6.03
048-XN38	0.00	93.42	0.16	0.36	856920.17	59.57	0.06	0.45	0.68	0.57	0.08	0.30	0.53	549.32	19.76	524.38	3.04	529.01	4.66	4.54
050-XN40	0.01	97.67	0.35	0.26	289215.97	12.38	0.06	0.56	0.71	0.68	0.09	0.36	0.52	561.30	24.29	542.94	3.71	546.43	5.74	3.27
058-XN44	0.05	361.32	0.17	0.47	33028.48	7.07	0.06	0.35	0.67	0.63	0.08	0.50	0.80	552.26	15.24	512.73	4.95	519.99	5.13	7.16
061-XN47	0.03	330.31	0.19	0.29	51788.47	16.31	0.06	0.76	0.66	1.06	0.08	0.73	0.69	554.23	32.84	504.64	7.11	513.65	8.56	8.95
007-XN5	0.01	134.95	0.24	0.27	122980.52	7.91	0.06	0.31	0.68	0.46	0.09	0.30	0.66	526.09	13.62	526.03	3.04	525.99	3.77	0.01

011-XN9	0.31	2121.09	0.16	1.23	5100.61	6.62	0.06	0.99	0.68	1.16	0.08	0.59	0.51	614.08	42.39	503.37	5.73	523.79	9.49	18.03
016-XN12	0.00	38.60	0.16	0.32	3161687.70	29.46	0.06	0.84	0.65	1.11	0.08	0.70	0.63	516.15	36.78	510.08	6.86	511.14	8.86	1.18
033-XN25	0.07	793.44	0.26	0.29	21536.05	4.90	0.06	0.44	0.74	0.56	0.09	0.31	0.55	586.59	19.20	554.93	3.30	561.13	4.85	5.40
037-XN29	0.01	120.81	0.40	0.42	276380.95	18.53	0.06	0.43	0.70	0.54	0.09	0.29	0.54	500.99	18.74	546.75	3.05	537.94	4.49	-9.13
045-XN35	0.11	1038.86	0.23	0.52	14379.46	4.76	0.06	0.34	0.67	0.57	0.08	0.43	0.76	619.22	14.64	497.27	4.15	519.59	4.64	19.69
056-XN42	0.01	86.53	0.16	0.45	272637.80	34.88	0.06	0.35	0.57	0.70	0.07	0.59	0.84	521.35	15.32	444.16	5.06	456.83	5.16	14.80
057-XN43	0.01	237.56	0.50	0.32	175668.55	10.25	0.06	0.42	0.59	0.70	0.08	0.54	0.77	434.99	18.80	478.48	4.95	471.00	5.28	-10.00
059-XN45	0.02	231.93	0.30	0.20	90405.58	8.03	0.06	0.42	0.63	0.68	0.08	0.51	0.75	513.64	18.57	490.10	4.79	494.23	5.31	4.58
060-XN46	0.17	956.57	0.13	0.26	9092.10	4.46	0.06	0.42	0.69	0.72	0.08	0.57	0.79	594.04	18.23	517.86	5.66	532.13	5.99	12.82
063-XN49	0.00	78.07	0.34	0.37	1265494.30	54.27	0.06	0.46	0.67	1.00	0.08	0.87	0.87	501.46	20.17	523.41	8.79	519.29	8.11	-4.38
Discordant data																				
006-XN4	0.60	3176.38	0.10	0.33	2587.58	7.55	0.07	0.82	0.71	1.11	0.07	0.73	0.66	1023.75	33.21	438.64	6.17	545.97	9.36	57.15
020-XN16	0.27	823.05	0.07	0.77	5761.75	3.72	0.06	1.46	0.62	1.94	0.07	1.27	0.66	662.45	61.75	456.48	11.23	492.23	15.08	31.09
022-XN18	0.20	3694.96	0.42	0.19	7604.84	5.45	0.06	0.85	0.60	1.13	0.07	0.74	0.65	603.82	36.48	452.71	6.44	478.41	8.63	25.03
029-XN21	0.72	9418.42	0.29	0.57	2171.07	7.06	0.07	0.54	0.77	0.75	0.08	0.50	0.66	1047.13	21.81	469.15	4.53	581.09	6.66	55.20
031-XN23	0.09	1303.41	0.30	0.41	16481.20	6.80	0.06	0.25	0.62	0.47	0.07	0.37	0.78	591.86	10.73	465.77	3.31	487.62	3.63	21.30
036-XN28	0.29	2677.27	0.22	0.98	5441.86	3.97	0.06	0.58	0.68	1.10	0.08	0.92	0.84	630.60	24.90	501.21	8.86	525.10	8.98	20.52
043-XN33	0.33	3759.92	0.22	0.63	4767.38	10.82	0.07	0.53	0.56	1.00	0.06	0.83	0.84	855.50	21.74	379.39	6.13	454.60	7.29	55.65
047-XN37	0.95	2113.99	0.05	2.07	1640.89	1.29	0.07	0.84	0.65	1.25	0.07	0.90	0.73	890.65	34.66	427.29	7.48	508.07	9.94	52.02
055-XN41	0.01	250.46	0.92	0.34	246554.35	7.67	0.05	0.50	0.56	0.75	0.08	0.54	0.72	282.43	22.91	482.53	5.04	449.23	5.47	-70.85
Data discarded by high analytical error																				
003-XN1	0.00	670.69	0.14	0.35	1074965.31	51.97	0.06	0.51	0.71	1.61	0.09	1.52	0.94	538.77	22.12	543.63	15.84	542.64	13.49	-0.90
005-XN3	0.21	1987.94	0.23	0.28	7530.21	3.80	0.06	0.42	0.72	0.51	0.09	0.24	0.47	641.44	17.99	531.27	2.43	552.54	4.31	17.18

009-XN7	0.35	3924.36	0.23	0.53	4484.46	8.20	0.06	0.79	0.61	2.38	0.08	2.24	0.94	559.15	34.32	467.74	20.23	483.49	18.26	16.35
015-XN11	0.37	5404.50	0.34	0.55	4218.46	5.35	0.06	1.22	0.69	5.52	0.08	5.38	0.97	696.40	51.67	492.58	50.95	530.31	45.12	29.27
017-XN13	0.08	3250.06	0.22	0.90	19799.06	35.34	0.06	2.23	0.63	2.33	0.08	0.67	0.29	441.09	97.59	504.88	6.51	493.46	18.14	-14.46
023-XN19	1.26	8283.19	0.16	1.56	1241.72	2.82	0.07	2.29	0.59	3.43	0.06	2.55	0.74	952.55	92.12	375.99	18.61	468.63	25.57	60.53
030-XN22	1.11	6171.27	0.12	0.87	1405.72	7.47	0.08	2.06	0.95	2.15	0.09	0.60	0.28	1172.29	80.60	539.90	6.24	678.90	21.22	53.94
034-XN26	0.28	913.68	0.06	0.31	5663.02	11.57	0.07	0.97	0.76	1.04	0.08	0.36	0.35	884.57	39.71	497.32	3.48	572.68	9.12	43.78
035-XN27	0.00	90.73	0.14	0.33	431940.77	71.47	0.06	0.46	0.68	0.54	0.09	0.24	0.44	521.60	20.18	526.57	2.43	525.59	4.44	-0.95
042-XN32	0.15	2172.30	0.22	0.32	10114.21	15.54	0.06	1.97	0.82	3.21	0.10	2.53	0.79	553.67	85.01	625.10	30.13	609.81	29.26	-12.90
044-XN34	0.11	809.31	0.13	0.53	14382.36	8.48	0.06	0.70	0.71	0.77	0.08	0.29	0.38	686.82	29.70	511.71	2.88	544.96	6.51	25.50
049-XN39	0.24	876.99	0.09	0.66	6497.68	3.29	0.06	0.91	0.61	1.06	0.07	0.51	0.48	562.27	39.47	464.94	4.57	481.65	8.08	17.31
062-XN48	0.00	56.28	0.27	0.38	3340205.00	42.08	0.06	0.38	0.68	0.97	0.09	0.87	0.90	542.48	16.79	526.59	8.81	529.53	7.95	2.93

Table 2: MC-LA-ICPMS U-Pb monazite data of SM1. Common lead corrections were applied in the calculation of isotope ratios and ages by using measured 204Pb. All errors are reported on a 2s basis. f206: fraction of common 206Pb.

Identifier	206* (%)	204Pb cps	206Pb mV1	Th/U	206Pb/204Pb	1s %	207Pb/206Pb	1s %	207Pb/235U	1s %	206Pb/238U	1s %	Rho	207Pb/206Pb	2s abs	206Pb/238U	2s abs	207Pb/235U	2s abs	% U-Pb disc
006-MZ4	0.02	59.18	0.02	17.05	76346.73	67.65	0.06	1.54	0.69	1.94	0.09	1.18	0.61	485.36	67.47	562.50	12.70	535.38	16.11	-15.89
007-MZ5	0.06	95.85	0.04	10.09	27705.61	9.76	0.06	1.52	0.68	2.03	0.09	1.35	0.66	441.05	66.99	562.79	14.54	527.33	16.66	-27.60
009-MZ7	0.05	61.01	0.02	14.60	30362.60	26.15	0.05	1.99	0.67	2.15	0.09	0.79	0.37	357.35	88.81	573.37	8.66	520.01	17.38	-60.45
010-MZ8	0.03	57.04	0.02	14.23	54809.41	56.12	0.05	2.48	0.66	2.61	0.09	0.81	0.31	298.64	111.31	579.83	9.02	514.27	20.97	-94.15
011-MZ9	0.01	27.53	0.01	17.70	212639.41	27.94	0.05	2.88	0.64	3.04	0.09	0.99	0.32	257.36	129.73	577.23	10.89	505.17	24.09	-124.29

012-				8.9	176453.1	40.		2.9		3.0		0.	0.		131.		10.		23.9	
MZ10	0.01	38.89	0.02	4	9	68	0.05	0	0.63	6	0.09	97	32	230.71	30	574.42	65	498.56	6	-148.98
015-				15.		10.		3.3		3.7		1.	0.		148.		17.		29.9	
MZ11	0.69	261.79	0.01	47	2262.70	83	0.05	8	0.66	5	0.09	62	43	394.83	28	554.96	17	512.96	8	-40.56
017-				14.	201964.6	27.		2.2		2.4		0.	0.		100.		9.9		18.8	
MZ13	0.01	23.45	0.01	90	0	32	0.05	3	0.63	2	0.09	93	38	269.77	68	558.60	1	493.77	0	-107.06
018-				15.		52.		2.0		2.2		0.	0.		90.8		10.		18.3	
MZ14	0.02	38.81	0.01	92	83499.03	71	0.05	3	0.67	5	0.09	98	43	326.51	5	584.30	92	522.50	2	-78.95
019-				10.	154485.1	35.		1.8		2.0		0.	0.		83.1		9.2		16.2	
MZ15	0.01	37.38	0.01	17	5	24	0.05	6	0.64	6	0.09	88	43	350.53	7	550.10	8	501.43	5	-56.93
020-				26.		42.		1.7		2.0		1.	0.		77.4		11.		17.0	
MZ16	0.02	36.48	0.01	42	89173.80	37	0.06	6	0.71	3	0.10	01	50	423.07	1	590.96	43	545.24	3	-39.68
022-				18.		38.		1.8		2.4		1.	0.		80.5		17.		20.4	
MZ18	0.02	30.09	0.01	56	73435.00	47	0.06	5	0.71	3	0.09	58	65	497.93	7	574.42	32	546.96	7	-15.36
023-				21.		45.		2.2		3.1		2.	0.		96.6		23.		26.1	
MZ19	0.02	31.43	0.01	46	93759.83	36	0.06	5	0.69	6	0.09	22	70	551.66	0	545.77	25	534.84	2	1.07
024-				16.	240412.5	23.		2.4		3.3		2.	0.		105.		23.		28.1	
MZ20	0.01	19.55	0.01	60	6	83	0.06	8	0.72	2	0.09	20	66	599.88	66	557.19	51	553.28	2	7.12
027-				16.	217064.7	23.		1.8		2.6		1.	0.		79.0		19.		22.4	
MZ21	0.01	20.33	0.01	78	9	40	0.06	7	0.71	9	0.09	93	72	664.48	2	527.71	54	541.99	3	20.58
030-				18.	223935.2	24.		1.4		1.8		1.	0.		64.6		12.		15.9	
MZ24	0.01	19.91	0.01	36	0	79	0.06	9	0.72	9	0.09	16	62	528.73	0	570.34	69	549.74	8	-7.87
031-				17.	175577.8	35.		1.6		2.0		1.	0.		71.2		12.		16.7	
MZ25	0.01	29.12	0.02	53	6	46	0.06	4	0.70	1	0.09	16	58	501.11	1	562.32	54	538.22	1	-12.21
032-				14.		14.		2.2		2.6		1.	0.		100.		14.		21.6	
MZ26	0.20	202.93	0.01	28	7695.86	05	0.05	8	0.69	3	0.09	32	50	411.45	28	573.84	49	530.23	4	-39.47
033-				15.	117550.4	42.		2.0		2.3		1.	0.		90.6		13.		20.1	
MZ27	0.01	37.58	0.02	74	7	37	0.06	8	0.71	9	0.09	19	50	467.34	3	580.52	23	545.78	1	-24.22
034-				17.	168086.1	31.		2.3		2.6		1.	0.		104.		12.		21.5	
MZ28	0.01	33.43	0.01	04	5	43	0.06	8	0.68	2	0.09	11	42	424.41	35	568.35	06	528.49	0	-33.92
035-				13.	157989.4	29.		2.5		2.7		1.	0.		111.		12.		22.4	
MZ29	0.01	28.46	0.01	57	5	03	0.06	4	0.66	8	0.09	13	41	414.56	76	555.47	00	516.90	3	-33.99
036-				20.	182455.0	37.		2.5		2.7		1.	0.		112.		12.		23.0	
MZ30	0.01	37.55	0.02	73	2	16	0.05	6	0.70	8	0.10	08	39	390.92	97	588.25	14	537.19	7	-50.48
005-				17.		66.		1.8		2.0		1.	0.		81.2		9.5		15.6	
MZ3	0.02	102.93	0.02	55	71040.52	26	0.05	3	0.58	9	0.08	01	48	396.97	0	493.99	9	466.28	0	-24.44
008-				17.		12.		1.9		2.0		0.	0.		79.9		8.1		18.6	
MZ6	0.58	682.66	0.02	04	2665.80	01	0.07	4	0.80	8	0.09	76	36	808.16	8	558.52	1	597.34	9	30.89
016-				19.		73.		2.7		2.8		0.	0.		126.		8.1		21.7	
MZ12	0.02	171.29	0.02	22	83897.42	81	0.05	6	0.60	6	0.09	76	27	183.32	12	559.71	4	480.11	9	-205.32
021-				17.		16.		1.7		2.0		1.	0.		75.1		12.		17.9	
MZ17	0.10	78.23	0.02	50	16300.91	54	0.06	2	0.77	4	0.10	10	54	489.50	1	617.79	90	578.22	2	-26.21
028-				16.		23.		1.5		2.1		1.	0.		67.3		16.		18.9	
MZ22	0.30	309.66	0.02	58	5107.42	88	0.06	9	0.79	4	0.10	43	67	656.54	4	586.89	03	588.44	9	10.61
029-				16.		56.		1.5		2.2		1.	0.		64.8		19.		19.9	
MZ23	0.03	57.99	0.02	45	53699.37	43	0.06	1	0.76	8	0.10	71	75	596.32	7	587.93	19	576.88	9	1.41

Data discarded by high analytical error																				
003-MZ1	0.96	923.91	0.02	10.37	1627.79	12.12	0.06	10.05	0.59	10.46	0.08	2.89	0.28	415.70	420.40	498.18	27.66	472.73	77.56	-19.84
Data discarded by high analytical error 204Pb																				
004-MZ2	5.13	4897.41	0.02	20.87	303.76	15.00	0.07	11.60	0.79	11.81	0.09	2.19	0.19	774.81	453.56	558.98	23.46	590.58	103.07	27.86

Table 3: MC-LA-ICPMS U-Pb zircon data of SM1. Common lead corrections were applied in the calculation of isotope ratios and ages by using measured 204Pb. All errors are reported on a 2s basis. f206: fraction of common 206Pb.

Identifier	206* (%)	204Pb cps	206Pb mV1	Th/U	206Pb/204Pb	1s %	207Pb/206Pb	1s %	207Pb/235U	1s %	206Pb/238U	1s %	Rho	207Pb/206Pb	2s abs	206Pb/238U	2s abs	207Pb/235U	2s abs	% U-Pb disc
004-ZR2	0.00	4.25	0.01	0.90	454728.60	20.50	0.10	0.53	3.92	0.94	0.29	0.68	0.73	1602.87	19.71	1628.21	19.59	1617.25	15.14	-1.58
006-ZR4	0.01	5.63	0.01	0.54	248630.68	9.83	0.10	0.52	3.65	0.90	0.27	0.63	0.70	1582.21	19.40	1545.46	17.26	1561.11	14.24	2.32
009-ZR7	0.00	9.92	0.01	1.03	395064.93	13.79	0.10	0.43	3.66	0.83	0.27	0.60	0.72	1589.38	16.15	1541.30	16.43	1561.75	13.15	3.03
011-ZR9	0.01	4.35	0.01	0.60	280963.70	13.06	0.10	0.64	3.66	0.97	0.27	0.74	0.65	1578.51	23.71	1551.12	17.52	1562.81	15.46	1.74
015-ZR11	0.00	21.41	0.02	0.70	340973.56	25.78	0.10	0.53	3.84	1.13	0.28	0.89	0.82	1623.63	19.70	1583.74	25.66	1600.99	17.99	2.46
016-ZR12	0.01	6.75	0.01	0.74	287153.04	12.90	0.10	0.52	3.77	0.94	0.28	0.63	0.82	1591.73	18.94	1584.02	19.31	1587.39	14.92	0.48
018-ZR13B	0.00	2.70	0.01	0.42	560637.51	10.51	0.10	0.43	4.07	0.83	0.30	0.60	0.74	1596.24	16.92	1688.97	24.72	1648.10	16.51	-5.81
024-ZR19	0.00	3.33	0.01	0.83	365848.81	6.73	0.10	0.54	3.88	0.88	0.29	0.65	0.74	1593.63	19.94	1622.70	15.84	1610.15	13.72	-1.82
027-ZR20	0.14	60.55	0.01	0.86	10951.06	34.01	0.10	0.56	3.90	1.09	0.28	0.69	0.63	1628.37	22.61	1602.14	19.23	1613.57	15.87	1.61
028-ZR21	0.01	28.00	0.01	0.74	168180.16	28.48	0.10	0.53	3.35	1.12	0.25	0.84	0.75	1533.00	19.61	1462.85	26.15	1491.78	18.41	4.58
029-ZR22	0.01	20.23	0.01	0.80	144288.25	25.91	0.10	0.52	3.64	1.03	0.27	0.72	0.70	1580.73	21.80	1540.52	19.90	1557.62	15.94	2.54
030-ZR23	0.01	5.64	0.01	0.91	264110.91	10.59	0.10	0.54	3.76	0.88	0.28	0.69	0.78	1590.37	18.04	1581.21	16.24	1585.20	13.44	0.58
031-ZR24	0.01	13.47	0.01	1.01	178226.49	15.50	0.10	0.52	3.82	0.98	0.28	0.68	0.68	1608.94	19.65	1587.28	16.97	1596.67	14.11	1.35
032-ZR25	0.00	7.09	0.01	0.69	306888.57	16.83	0.10	0.54	4.07	1.02	0.30	0.87	0.87	1604.89	17.70	1683.47	31.68	1648.86	19.94	-4.90
033-ZR26	0.01	5.99	0.01	0.66	222275.05	11.13	0.10	0.52	3.70	0.95	0.27	0.69	0.69	1613.41	18.22	1538.85	16.18	1570.61	13.59	4.62

035-				0.5	375153.5	18.		0.6		1.1		0.9	0.		22.6		25.0		18.6	
ZR28	0.00	10.09	0.01	8	2	45	0.10	1	3.56	8	0.26	4	80	1612.97	2	1488.93	3	1540.97	5	7.69
043-				0.9	314617.5	9.2		0.4		1.0		0.8	0.		17.3		23.0		16.3	
ZR32	0.00	4.27	0.01	1	6	5	0.10	7	3.69	3	0.27	4	81	1591.83	5	1551.55	6	1568.75	4	2.53
045-				0.8	175459.1	13.		0.4		0.8		0.6	0.		18.3		16.8		13.8	
ZR34	0.01	9.91	0.00	8	7	26	0.10	9	3.72	7	0.27	1	70	1597.83	4	1557.56	3	1574.80	1	2.52
046-				0.8	280549.0	23.		0.4		1.2		1.0	0.		17.2		29.9		19.4	
ZR35	0.01	4.92	0.00	5	6	84	0.10	6	3.78	2	0.28	7	87	1589.35	0	1587.67	7	1588.45	9	0.11
047-				0.7	183768.8	20.		0.5		1.2		1.0	0.		21.3		27.3		19.2	
ZR36	0.01	11.80	0.01	6	0	46	0.10	7	3.55	2	0.26	1	83	1572.65	6	1512.49	0	1537.81	6	3.83
049-				0.5	225850.0	15.		0.5		0.8		0.5	0.		18.4		16.4		13.6	
ZR38	0.01	7.25	0.01	7	4	38	0.10	0	3.73	6	0.27	9	69	1601.53	7	1560.38	0	1578.01	8	2.57
052-				1.2		9.5		0.7		1.0		0.5	0.		28.9		15.7		16.3	
ZR41	0.28	116.13	0.01	5	5501.21	0	0.10	8	3.54	4	0.26	8	56	1572.79	1	1508.06	2	1535.26	9	4.12
055-				0.8	267554.1	26.		0.5		1.0		0.7	0.		18.8		21.7		15.9	
ZR42	0.01	9.12	0.01	0	3	60	0.10	1	3.78	0	0.28	7	78	1589.77	6	1588.59	8	1589.16	4	0.07
057-				0.8		5.8		0.7		1.9		1.7	0.		26.9		47.8		30.4	
ZR44	0.33	114.75	0.01	0	4707.81	7	0.10	3	3.79	1	0.27	3	90	1628.93	8	1562.00	5	1590.75	9	4.11
058-				0.9	185766.8	15.		0.4		0.8		0.6	0.		15.7		18.4		13.9	
ZR45	0.01	10.89	0.01	6	3	10	0.10	2	3.64	8	0.27	8	77	1594.56	4	1532.06	2	1558.58	6	3.92
060-				0.8	209187.2	30.		0.5		1.1		0.9	0.		21.5		24.2		18.2	
ZR47	0.01	26.42	0.01	2	7	44	0.10	7	3.16	9	0.24	7	82	1529.20	8	1392.72	9	1447.68	3	8.92
061-				0.7		20.		0.6		1.1		0.8	0.		24.0		23.3		18.0	
ZR48	0.13	85.88	0.01	7	11522.11	68	0.10	4	3.49	5	0.26	8	76	1577.59	2	1488.93	4	1525.98	9	5.62
068-				0.7	330094.8	11.		0.4		0.7		0.5	0.		15.1		15.2		12.3	
ZR53	0.00	4.20	0.01	3	5	11	0.10	0	3.75	7	0.28	4	70	1572.55	2	1588.21	9	1581.56	4	-1.00
069-				0.4	104462.8	21.		0.5		0.9		0.6	0.		21.0		17.8		14.9	
ZR54	0.01	20.54	0.00	4	9	29	0.10	6	3.63	4	0.27	6	70	1589.90	1	1531.63	7	1556.34	3	3.66
071-				0.8	330170.4	12.		0.4		0.7		0.5	0.		15.6		14.8		12.4	
ZR56	0.00	6.88	0.01	6	6	39	0.10	2	3.53	9	0.26	6	70	1580.84	6	1499.44	6	1533.58	4	5.15
072-				0.5	136266.5	17.		0.6		1.0		0.7	0.		22.7		21.4		16.8	
ZR57	0.01	10.21	0.00	3	5	10	0.10	1	3.59	7	0.27	9	74	1575.47	9	1525.95	7	1546.89	6	3.14
076-				0.0		68.		1.4		2.5		1.9	0.		65.8		20.2		20.0	
ZR61	0.02	93.60	0.01	4	67476.90	98	0.05	9	0.66	0	0.09	7	79	410.31	7	536.27	5	512.98	0	-30.70
079-				0.9	127869.1	19.		0.6		0.9		0.6	0.		22.5		17.4		15.2	
ZR62	0.01	16.36	0.01	4	1	19	0.10	1	3.68	6	0.27	4	67	1610.41	9	1534.20	8	1566.60	4	4.73
084-				0.6		30.		0.5		1.0		0.8	0.		19.7		22.8		16.9	
ZR67	0.05	137.71	0.02	9	30976.32	23	0.10	3	3.67	7	0.26	5	79	1636.45	6	1512.53	2	1565.03	7	7.57
087-				0.6		39.		0.6		1.0		0.6	0.		24.9		16.6		15.5	
ZR70	0.02	29.45	0.01	1	75754.39	23	0.10	7	3.30	0	0.25	4	65	1535.93	8	1444.02	7	1481.70	1	5.98
094-				0.8		16.		0.8		1.1		0.7	0.		29.8		20.6		18.5	
ZR73	0.27	96.80	0.01	0	5612.80	98	0.10	0	3.49	8	0.26	8	66	1585.62	6	1483.02	4	1525.85	2	6.47
100-				0.7	466852.5	27.		0.7		1.0		0.6	0.		26.1		17.6		16.2	
ZR79	0.00	8.71	0.01	2	0	29	0.10	0	3.56	3	0.26	6	64	1592.06	7	1505.25	3	1541.76	9	5.45
106-				0.2		5.9		0.6		1.1		0.8	0.		23.2		24.2		18.2	
ZR83	0.50	667.67	0.03	4	3100.58	3	0.10	3	3.72	5	0.27	9	77	1623.07	2	1540.69	6	1575.83	7	5.08

107-				0.8	190908.8	16.		0.6		1.0		0.7	0.		22.5		19.1		15.9	
ZR84	0.01	8.25	0.01	3	5	42	0.10	0	3.47	1	0.26	2	71	1568.58	3	1485.21	8	1519.97	0	5.32
108-				0.8	209080.8	14.		0.6		1.4		1.2	0.		24.8		32.3		22.6	
ZR85	0.01	6.84	0.01	6	6	52	0.10	6	3.38	5	0.25	4	85	1549.35	8	1463.20	0	1498.79	1	5.56
111-				0.5		6.1		0.8		1.1		0.6	0.		31.1		17.1		17.5	
ZR88	0.44	193.09	0.01	9	3511.01	1	0.10	3	3.54	1	0.26	4	57	1565.67	4	1514.73	8	1536.17	6	3.25
113-				0.7	194417.7	31.		0.6		1.1		0.8	0.		25.3		21.9		17.7	
ZR90	0.01	24.36	0.01	0	9	87	0.10	8	3.73	1	0.27	0	72	1611.36	6	1554.30	9	1578.72	5	3.54
114-				0.5		22.		0.7		1.1		0.7	0.		27.3		23.4		18.5	
ZR91	0.02	30.60	0.01	5	88379.10	03	0.10	4	4.06	4	0.30	9	69	1603.88	8	1679.50	1	1646.23	6	-4.71
117-				0.8		20.		0.7		1.1		0.7	0.		27.9		21.8		18.3	
ZR92	0.16	59.99	0.01	9	9892.86	96	0.10	6	3.86	4	0.28	8	68	1629.47	4	1586.92	2	1605.34	8	2.61
120-				0.8	138746.6	14.		0.7		1.2		0.8	0.		28.3		24.1		19.3	
ZR94B	0.01	8.22	0.00	7	7	73	0.10	6	3.80	1	0.28	6	71	1604.98	8	1582.54	9	1592.25	7	1.40
121-				1.0		6.3		0.7		1.1		0.8	0.		27.6		22.6		18.6	
ZR95	0.36	129.59	0.01	6	4300.63	4	0.10	5	3.80	7	0.27	2	70	1630.50	7	1563.64	2	1592.39	7	4.10
123-				0.8	168203.1	21.		0.6		0.9		0.6	0.		22.6		17.8		15.3	
ZR97	0.01	19.38	0.01	8	9	69	0.10	1	3.55	7	0.26	6	68	1577.39	0	1512.03	9	1539.54	5	4.14
124-				0.8		8.8		0.6		1.0		0.8	0.		22.4		19.8		16.4	
ZR98	0.19	62.77	0.01	3	8205.34	5	0.09	0	2.96	9	0.23	3	76	1522.86	6	1316.60	0	1397.43	7	13.54
126-				0.8	230216.9	21.		0.6		1.0		0.6	0.		25.7		18.5		16.4	
ZR100	0.01	6.04	0.01	8	8	39	0.10	9	3.68	3	0.27	7	65	1582.31	9	1555.88	2	1567.18	2	1.67
003-				0.7	485420.6	8.3		0.4		0.9		0.7	0.		14.8		21.8		15.0	
ZR1	0.00	3.77	0.01	8	2	5	0.10	0	3.81	4	0.28	7	82	1570.52	6	1611.92	4	1594.12	6	-2.64
004-				0.9	454728.6	20.		0.5		0.9		0.6	0.		19.7		19.5		15.1	
ZR2	0.00	4.25	0.01	0	0	50	0.10	3	3.92	4	0.29	8	73	1602.87	1	1628.21	9	1617.25	4	-1.58
007-				0.0		88.		1.3		2.3		1.8	0.		58.5		22.8		21.6	
ZR5	0.02	182.24	0.02	5	99929.35	91	0.06	5	0.85	3	0.11	6	80	555.59	4	645.18	3	625.67	6	-16.13
012-				0.7	182674.2	17.		0.7		1.1		0.7	0.		25.8		19.2		17.2	
ZR10	0.01	25.20	0.01	7	7	24	0.10	0	3.34	1	0.24	7	70	1644.02	3	1385.63	2	1490.97	0	15.72
020-				0.1		8.5		0.6		1.2		0.9	0.		25.1		21.1		18.2	
ZR15	0.32	87.21	0.01	5	4767.73	0	0.09	7	2.61	5	0.20	9	79	1525.94	4	1171.04	7	1302.47	8	23.26
022-				0.6	281462.4	30.		0.9		2.3		2.1	0.		35.8		50.2		35.2	
ZR17	0.01	5.18	0.00	0	8	12	0.09	5	2.88	6	0.22	3	90	1489.35	1	1305.77	2	1377.10	8	12.33
023-				0.6		42.		0.6		1.0		0.7	0.		24.2		18.7		16.2	
ZR18	0.06	41.15	0.01	4	24403.21	24	0.10	5	3.39	4	0.25	2	69	1589.62	8	1441.54	0	1502.59	9	9.32
034-				0.5		10.		1.0		1.4		0.8	0.		39.8		20.0		22.0	
ZR27	1.01	382.28	0.01	7	1528.22	56	0.10	9	3.33	2	0.23	3	59	1705.72	5	1339.19	7	1487.51	4	21.49
036-				0.9		30.		0.5		1.0		0.7	0.		21.8		18.6		15.9	
ZR29	0.02	33.65	0.01	5	73972.64	98	0.10	9	3.09	4	0.23	8	75	1580.11	5	1330.84	9	1429.76	2	15.78
042-				0.9		29.		0.5		0.9		0.7	0.		20.3		18.1		15.1	
ZR31	0.02	25.38	0.01	4	77098.48	07	0.10	5	3.37	7	0.25	1	73	1602.20	9	1424.35	0	1497.38	3	11.10
050-				0.6		9.0		1.3		1.6		0.8	0.		49.4		16.6		23.1	
ZR39	0.32	99.31	0.01	6	4851.82	1	0.10	3	2.43	2	0.18	4	52	1564.16	7	1076.04	8	1250.28	3	31.21
051-				0.1	165479.8	25.		0.5		1.2		1.0	0.		22.1		25.1		18.9	
ZR40	0.01	47.38	0.01	6	4	45	0.10	9	3.27	3	0.24	1	82	1596.56	3	1388.75	4	1473.05	9	13.02

063-				0.7		15.		0.6		1.0		0.6	0.		25.8		18.5		16.2	
ZR50	0.46	166.32	0.01	6	3323.21	49	0.10	9	3.96	1	0.30	3	63	1567.86	8	1671.41	9	1626.12	9	-6.60
080-				0.3		3.8		0.9		2.1		1.9	0.		36.1		39.0		31.8	
ZR63	1.10	240.68	0.01	5	1414.29	6	0.10	8	2.60	9	0.19	2	88	1636.10	4	1107.11	4	1300.75	5	32.33
083-				0.0		2.8		0.5		0.9		0.7	0.		23.0					
ZR66	1.14	912.02	0.02	1	1361.38	9	0.07	6	0.87	8	0.09	2	73	892.72	2	566.90	7.79	636.68	9.28	36.50
086-				0.6		13.		1.0		1.7		1.2	0.		39.3		23.2		24.9	
ZR69	0.90	464.68	0.01	3	1728.96	17	0.11	9	2.60	1	0.17	7	74	1847.85	0	993.57	8	1299.51	6	46.23
095-				0.3		5.6		0.9		1.8		1.4	0.		36.6		31.6		26.5	
ZR74	0.50	244.89	0.01	7	3097.65	2	0.10	8	2.65	1	0.20	8	82	1553.35	0	1173.71	2	1315.03	1	24.44
110-				0.5	151836.1	25.		0.5		1.1		0.9	0.		19.9		27.1		18.1	
ZR87	0.01	11.32	0.00	0	2	94	0.10	3	4.03	2	0.30	1	81	1568.29	1	1695.97	4	1639.77	2	-8.14
112-				1.0		14.		0.6		1.0		0.7	0.		23.3		19.1		16.3	
ZR89	0.21	100.85	0.01	3	7501.03	21	0.10	3	3.59	3	0.26	3	70	1643.16	8	1476.56	7	1546.44	3	10.14
122-				0.6		15.		0.7		1.0		0.6	0.		27.8		15.7		15.8	
ZR96	0.27	144.82	0.01	1	5791.88	37	0.09	4	3.25	3	0.25	1	59	1504.85	5	1445.22	0	1469.59	8	3.96
125-				0.4	317082.4	21.		0.7		1.1		0.7	0.		28.9		20.4		17.9	
ZR99	0.00	14.83	0.01	5	8	66	0.10	8	3.75	3	0.28	3	64	1563.60	8	1594.92	8	1581.54	6	-2.00
Discordant data																				
067-				0.5		19.		2.4		3.3		2.2	0.		84.8		50.3		52.7	
ZR52	0.44	274.30	0.01	2	3499.85	16	0.13	4	3.73	4	0.21	4	67	2067.82	9	1236.37	5	1576.86	3	40.21
096-				0.7		77.		1.3		1.7		1.1	0.		42.7		33.4		31.9	
ZR75	0.29	581.04	0.00	6	5312.33	06	0.20	2	8.22	8	0.30	3	64	2832.26	9	1676.64	3	2255.82	8	40.80
101-				0.9		12.		2.3		3.1		2.0	0.		80.1		44.2		51.0	
ZR80	0.97	320.89	0.00	6	1593.57	89	0.15	7	4.02	8	0.20	9	66	2321.14	6	1159.76	5	1637.90	7	50.03
Data discarded by high analytical error																				
005-				0.1		37.		4.5		4.6		0.6	0.		197.				40.5	
ZR3	0.24	285.48	0.01	5	6355.59	07	0.06	6	0.78	2	0.10	3	14	416.26	48	626.82	7.53	583.13	5	-50.58
010-				0.7		56.		0.5		2.1		2.0	0.		20.3		46.0		32.8	
ZR8	0.06	118.51	0.01	1	27033.52	63	0.10	5	3.04	6	0.21	6	95	1708.53	0	1230.40	6	1416.53	0	27.98
017-				0.0		12.		1.4		1.6		0.8	0.		59.3				14.4	
ZR13N	0.24	189.91	0.02	8	6556.80	59	0.06	1	0.75	6	0.09	0	48	700.67	3	537.92	8.26	570.15	3	23.23
019-				0.2		12.		0.6		2.4		2.2	0.		25.7		40.9		32.8	
ZR14	0.26	76.34	0.00	2	5866.10	84	0.09	8	2.11	0	0.16	7	95	1504.95	1	973.39	8	1151.79	1	35.32
021-				0.3		8.1		0.7		3.2		3.1	0.		25.7		72.8		49.2	
ZR16	0.31	231.33	0.02	5	4996.58	9	0.10	0	3.11	4	0.22	4	97	1673.83	3	1281.45	2	1436.39	0	23.44
041-				0.6		28.		2.5		6.9		6.4	0.		101.		66.7		64.4	
ZR30	0.03	79.64	0.01	5	49868.46	00	0.07	3	0.86	7	0.09	8	93	978.14	31	538.02	4	630.59	1	45.00
044-				3.6	725359.0	18.		1.0		3.9		3.7	0.		40.6		60.3		49.2	
ZR33	0.00	11.40	0.02	2	9	27	0.09	6	1.69	0	0.14	4	96	1328.75	7	864.80	3	1006.35	1	34.92
056-				0.6		75.		1.6		7.9		7.8	0.		64.8		50.3		58.2	
ZR43	0.07	163.94	0.01	5	23726.99	20	0.08	5	0.57	9	0.05	1	98	1168.10	4	331.18	0	460.01	6	71.65
059-				0.6		94.		12.		12.		1.2	0.		520.		27.3		153.	
ZR46	0.14	533.61	0.00	0	10684.92	54	0.06	78	1.57	85	0.20	6	10	478.66	18	1183.28	0	960.16	64	-147.20

062-				1.2		4.9		0.7		3.6		3.5	0.		28.5		76.0		52.8	
ZR49	0.61	182.23	0.01	5	2536.64	5	0.10	6	2.64	3	0.20	3	97	1529.95	3	1181.37	6	1311.10	1	22.78
064-				1.3		11.		1.0		24.		24.	1.		37.6		194.		233.	
ZR51	0.83	256.99	0.00	6	1889.70	03	0.11	4	1.02	20	0.07	17	00	1802.71	8	418.34	35	713.32	98	76.79
070-				0.7		65.		3.1		3.3		1.0	0.		104.		31.2		57.7	
ZR55	0.14	387.50	0.00	5	10897.08	64	0.16	3	6.67	2	0.31	3	31	2418.32	41	1735.80	7	2068.49	6	28.22
073-				0.7		6.8		0.6		4.6		4.5	0.		23.7		89.6		65.8	
ZR58	0.55	256.62	0.01	1	2821.57	8	0.10	4	2.50	2	0.18	6	99	1628.71	1	1070.31	0	1271.06	8	34.28
075-				0.7		7.6		0.5		1.9		1.8	0.		19.6		48.0		30.5	
ZR60	0.31	332.98	0.02	3	4978.88	1	0.10	3	3.66	3	0.26	2	94	1673.80	1	1480.23	4	1561.82	7	11.57
081-				0.6		18.		0.7		6.2		6.2	0.		27.4		89.3		80.1	
ZR64	0.36	223.03	0.01	6	4305.15	47	0.10	5	1.80	6	0.13	0	99	1686.05	9	766.21	1	1045.28	0	54.56
082-				0.0		6.2		3.0		3.1		0.6	0.		122.				30.5	
ZR65	1.36	932.31	0.01	2	1142.48	8	0.07	9	0.91	8	0.09	6	21	1046.23	14	549.35	6.91	656.96	3	47.49
085-				0.6		34.		1.6		1.8		0.6	0.		61.3		17.8		28.6	
ZR68	0.02	358.29	0.01	9	66318.11	23	0.10	5	3.55	2	0.27	6	36	1565.83	9	1520.38	0	1539.55	2	2.90
093-				0.6		50.		2.1		2.4		0.9	0.		80.8		25.9		38.1	
ZR72	0.08	66.40	0.00	3	20106.30	95	0.10	9	3.74	0	0.28	2	38	1564.51	5	1591.64	9	1580.07	1	-1.73
097-		7837.9		0.0		24.		3.8		3.9		0.7	0.		116.				63.0	
ZR76	1.11	0	0.02	2	1397.39	24	0.30	5	4.01	4	0.10	4	19	3486.13	72	591.09	8.38	1636.91	7	83.04
098-				0.3		30.		3.1		6.9		6.1	0.		115.		164.		106.	
ZR77	0.03	148.62	0.01	1	45297.17	56	0.10	4	3.58	2	0.26	5	89	1586.84	32	1514.43	97	1544.96	94	4.56
099-				0.4		6.2		0.7		3.0		2.9	0.		28.4		37.4		35.3	
ZR78	0.53	202.36	0.01	8	2928.84	0	0.09	5	1.39	2	0.11	0	96	1440.89	8	680.82	3	886.20	9	52.75
109-				0.8		36.		0.7		4.2		4.1	0.		28.3		102.		65.3	
ZR86	0.03	50.44	0.01	3	59022.82	36	0.10	7	3.25	8	0.23	9	98	1637.73	5	1354.47	02	1468.67	6	17.30
118-				0.7		10.		0.7		8.7		8.6	1.		27.2		114.		108.	
ZR93	0.39	131.04	0.01	0	3945.34	55	0.11	5	1.68	3	0.11	9	00	1737.74	9	698.48	53	1000.29	15	59.81
Data discarded by high 204Pb content																				
008-				0.5		2.0		0.7		1.3		1.0	0.		26.8		22.4		20.4	
ZR6	1.82	640.68	0.01	4	851.65	6	0.11	4	3.03	5	0.20	6	79	1827.27	1	1156.58	9	1414.41	8	36.70
048-		1347.8		1.0		8.7		2.4		3.0		1.7	0.		73.7		58.7		56.5	
ZR37	7.35	5	0.00	6	206.92	5	0.31	3	15.50	0	0.36	3	58	3541.68	6	1971.32	0	2846.36	0	44.34
074-				0.9		20.		16.		16.		2.0	0.		605.		53.1		231.	
ZR59	1.91	967.20	0.01	9	806.60	76	0.07	58	2.62	71	0.26	2	12	1038.47	90	1473.56	6	1305.33	78	-41.90
088-		3844.1		0.0		11.		9.3		9.7		2.9	0.		358.		23.3		76.9	
ZR71	6.01	5	0.01	2	259.39	13	0.07	1	0.65	7	0.07	2	30	973.91	19	413.41	6	510.74	2	57.55
102-		1031.9		0.3		4.3		1.3		9.1		9.0	0.		50.6		94.6		101.	
ZR81	2.01	4	0.01	7	773.40	9	0.11	9	1.29	2	0.09	1	99	1721.03	3	550.22	6	843.41	92	68.03
105-		2428.6		0.4		5.7		2.0		3.7		3.1	0.		73.4		54.7		54.3	
ZR82	2.29	4	0.02	0	676.51	4	0.12	8	2.57	7	0.16	2	83	1926.51	9	945.95	8	1292.77	3	50.90
119-				2.4		5.7		2.0		4.1		3.5	0.		69.3		41.4		54.6	
ZR94N	2.17	552.83	0.01	9	716.84	4	0.14	4	1.99	0	0.10	3	86	2273.78	6	616.05	7	1111.70	1	72.91

1

Annex 2

Fig 1: A,B and C- euhedral to anhedral tetragonal dipyramidal short prisms of light yellow to dark brown xenotime (~ 400-1000 µm); D-euhedral to anhedral prismatic reddish brown to light yellow monazite (~ 350-1200 µm)

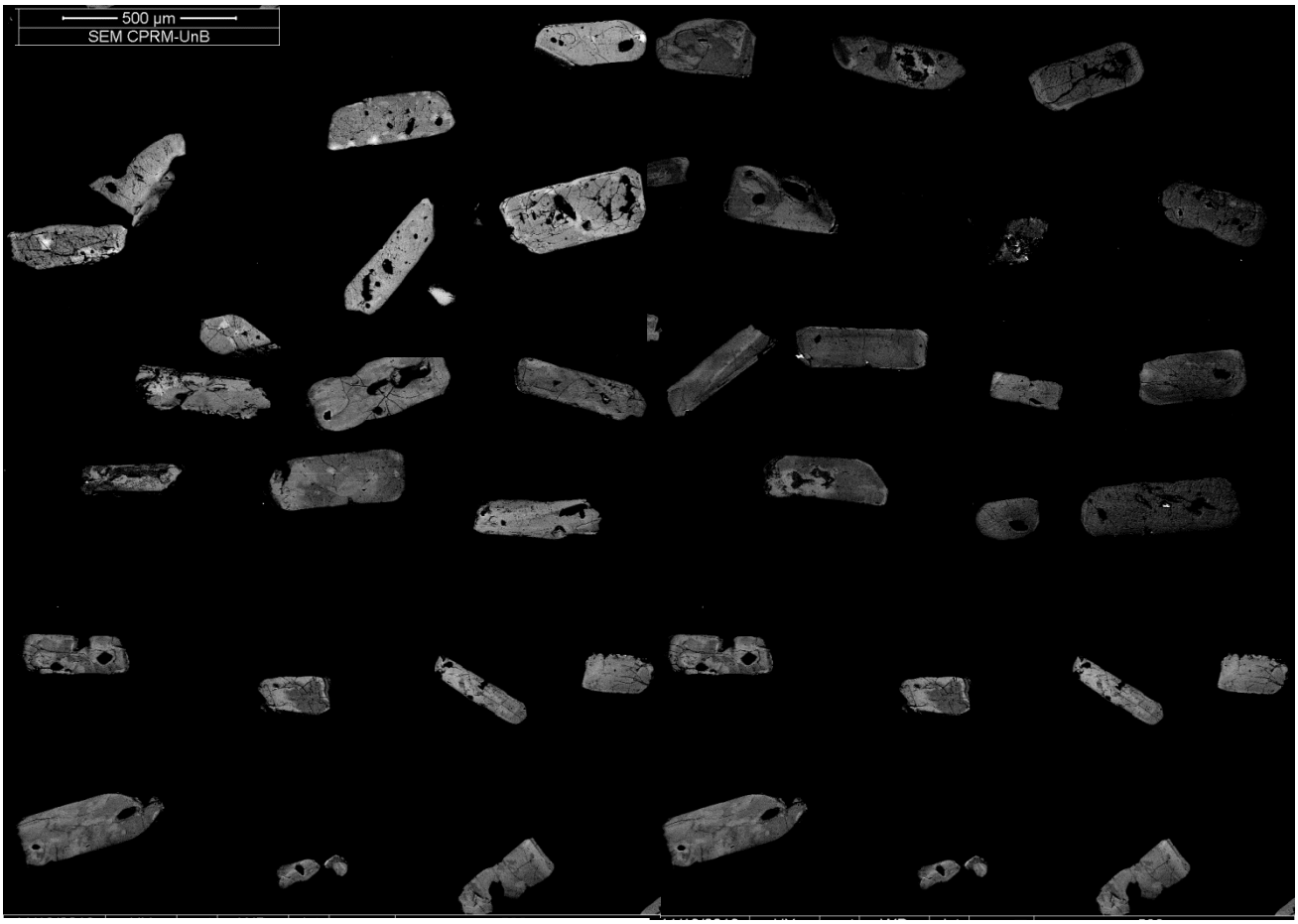

Fig2: Backscattered electron images of detrital euhedral to anhedral prismatic zircon (~ 100-200 µm).